

Circular resistor networks for electrical impedance tomography with partial boundary measurements.

L. Borcea¹, V. Druskin² and A.V. Mamonov¹

¹Computational and Applied Mathematics, Rice University,
MS 134, 6100 Main St. Houston, TX 77005-1892, USA

²Schlumberger Doll Research Center,
One Hampshire St., Cambridge, MA 02139-1578, USA

E-mail: borcea@rice.edu, druskin1@slb.com and mamon@rice.edu

Abstract. We introduce an algorithm for the numerical solution of electrical impedance tomography (EIT) in two dimensions, with partial boundary measurements. The algorithm is an extension of the one in [11, 49] for EIT with full boundary measurements. It is based on resistor networks that arise in finite volume discretizations of the elliptic partial differential equation for the potential, on so-called optimal grids that are computed as part of the problem. The grids are adaptively refined near the boundary, where we measure and expect better resolution of the images. They can be used very efficiently in inversion, by defining a reconstruction mapping that is an approximate inverse of the forward map, and acts therefore as a preconditioner in any iterative scheme that solves the inverse problem via optimization. The main result in this paper is the construction of optimal grids for EIT with partial measurements by extremal quasiconformal (Teichmüller) transformations of the optimal grids for EIT with full boundary measurements. We present the algorithm for computing the reconstruction mapping on such grids, and we illustrate its performance with numerical simulations. The results show an interesting trade-off between the resolution of the reconstruction in the domain of the solution and distortions due to artificial anisotropy induced by the distribution of the measurement points on the accessible boundary.

1. Introduction

This paper is concerned with the numerical approximation of solutions of the inverse problem of electrical impedance tomography (EIT) in two dimensions, with partial boundary measurements. In EIT [13, 6] we wish to determine the positive and bounded coefficient σ in the elliptic equation

$$\nabla \cdot (\sigma(x)\nabla u(x)) = 0, \quad x \in \Omega, \quad (1.1)$$

from measurements of the Dirichlet-to-Neumann (DtN) map Λ_σ . The domain Ω is an open, bounded and simply connected set in \mathbb{R}^2 , with boundary \mathcal{B} . By the Riemann mapping theorem all such sets are conformally equivalent, so we take from now on $\Omega = \mathbb{D}$, the unit disk in \mathbb{R}^2 . The coefficient σ is called the conductivity, and $u \in H^1(\mathbb{D})$ is the potential, satisfying Dirichlet boundary conditions

$$u(x)|_{\mathcal{B}} = \phi(x), \quad (1.2)$$

for $\phi \in H^{1/2}(\mathcal{B})$. The DtN map $\Lambda_\sigma : H^{1/2}(\mathcal{B}) \rightarrow H^{-1/2}(\mathcal{B})$ takes the boundary potential ϕ and returns the normal boundary flux (current)

$$\Lambda_\sigma \phi = \sigma \frac{\partial u}{\partial \nu} \Big|_{\mathcal{B}}, \quad (1.3)$$

where ν is the outward unit normal at \mathcal{B} .

EIT with full boundary measurements corresponds to the case where all possible boundary excitations and measurements are available. We consider the EIT problem with partial boundary measurements [27] on the *accessible* subset \mathcal{B}_A of the boundary. The *inaccessible* boundary $\mathcal{B}_I = \mathcal{B} \setminus \mathcal{B}_A$ is assumed grounded \ddagger . The problem is to determine σ given the knowledge of the operator $\Lambda_\sigma^A : H^{1/2}(\mathcal{B}_A) \rightarrow H^{-1/2}(\mathcal{B}_A)$ defined as

$$\Lambda_\sigma^A (\phi|_{\mathcal{B}_A}) = \sigma \frac{\partial u}{\partial \nu} \Big|_{\mathcal{B}_A}, \quad (1.4)$$

where ϕ from (1.2) obeys an additional condition $\text{supp } \phi \subset \mathcal{B}_A$.

The uniqueness of solution of the EIT problem with full boundary measurements was established in [48, 42] under some smoothness assumptions on σ , and more recently in [2], for bounded σ . The uniqueness of solution of the EIT problem with partial boundary measurements, and for real-analytic or piecewise real-analytic σ , follows from [21, 22, 33, 34]. The first global uniqueness result was obtained more recently in [12], in three or more dimensions and for a restrictive measurement setup. The uniqueness result that is relevant to our formulation is given in [27], for σ of class $C^{3+\epsilon}$ in the closure of the domain, where $\epsilon > 0$.

Even with full boundary measurements the EIT problem is unstable. There exist stability estimates [1, 4] under some assumptions on the regularity of σ , but they cannot be better than logarithmic [40]. That is, given two sufficiently regular conductivities σ_1 and σ_2 , the following estimate holds

$$\|\sigma_1 - \sigma_2\|_{L^\infty(\mathbb{D})} \leq C \left| \log \|\Lambda_{\sigma_1} - \Lambda_{\sigma_2}\|_{H^{1/2}(\mathcal{B}) \rightarrow H^{-1/2}(\mathcal{B})} \right|^{-\alpha}, \quad (1.5)$$

where C and α are positive constants. See also the stability estimates in [32], that deal with cases where due to noise, the measured data is no longer a DtN map. These estimates are also of logarithmic type. Thus, one needs an exponentially good fit of the data in order to obtain a noticeable improvement of the estimated conductivity. We are not aware of any stability results for EIT with partial boundary measurements (1.4). There is a stability estimate in dimensions three or higher for a less general measurement setup [26], which is of log-log type. Nevertheless, it is clear that if stability estimates existed, they could not be better than the estimate (1.5) for the full boundary measurements case.

Naturally, any numerical method that seeks an approximate solution of the EIT problem uses finitely many measurements of potentials and boundary currents. Despite having a finite number of measurements, we say that we have full boundary data when the measurement points are distributed on the entire boundary. By partial measurements we mean that the points are confined to the accessible boundary \mathcal{B}_A . The uniqueness and stability of the numerical estimate of σ depends on its

\ddagger We make this assumption so that we can use existing results on the solvability of the discrete and continuum inverse problems. The case of insulated boundary $\sigma \frac{\partial u}{\partial \nu} \Big|_{\mathcal{B}_I} = 0$, which may arise in applications, can be handled using convex duality.

parametrization. If we seek too many parameters, the numerical method becomes unstable, and it must be regularized [25] using for example prior assumptions on σ . We assume no such prior information, and use instead a regularization approach based on sparse parametrizations of the conductivity.

Regularization by sparse representation of the unknown in some preassigned basis of functions has been proposed and analyzed for linear inverse problems in [16]. The question is how to choose the basis and how to obtain fast inversion algorithms that can work for the nonlinear and exponentially ill posed EIT problem.

We follow the approach in [11, 49] and parametrize the unknown conductivity on adaptive grids which we call *optimal*. The number of grid points is limited by the precision of the measurements and their location is determined as part of the inverse problem. The resulting grids are refined near the boundary, where we make the measurements, and they are coarse inside the domain, thus capturing the gradual loss of resolution of the reconstructions away from \mathcal{B} .

Other adaptive grids for EIT have been proposed in [31, 38, 37]. They are called *distinguishability* grids because they are constructed with a linearization argument that looks for the smallest support of a perturbation $\delta\sigma$ at a given location in the domain, that can be distinguished at the boundary from a constant σ .

The optimal grids considered in [11, 49] and in this paper are computed with an approach based on rational approximation techniques. They are called optimal because they give spectral accuracy of the DtN map with finite volumes on coarse grids. Optimal grids were introduced and analyzed in [3, 23, 24, 29], for forward problems. The first inversion method on optimal grids was proposed in [7], for Sturm-Liouville inverse spectral problems in one dimension. Then, it was shown in [8] that optimal grids provide a necessary and sufficient condition for convergence of solutions of discrete inverse spectral problems to the true solution of the continuum problem.

The first inversion method on optimal grids for two dimensional EIT with full boundary measurements was proposed and analyzed in [11, 49]. It is based on the rigorous theory of discrete inverse problems for *circular resistor networks* developed in [14, 15, 28, 17, 18]. The circular networks arise in the discretization of equation (1.1) with a five point stencil finite volumes scheme on the optimal grids computed as part of the inverse problem. The networks are *critical*, i.e., they have no redundant connections, so that they can be determined uniquely by the discrete boundary measurements. They can also be recovered from the measurements with a fast, non-iterative layer peeling algorithm [14] that can be regularized by restricting the number of layers. This implies restricting the number of grid points.

The algorithm in [11, 49] approximates the solution of the EIT problem with full boundary measurements, as follows: First, it uses the optimal grids and the resistor networks to define a nonlinear *reconstruction* mapping \mathcal{Q}_n from the boundary data space to the space of bounded and positive conductivity functions. This mapping is called a *reconstruction* because it is an approximate inverse of the forward map, which takes the conductivity to the data. Then, it uses \mathcal{Q}_n as a preconditioner in a Gauss-Newton iteration for estimating σ . The iteration converges in one or two steps, and the method is fast, because the evaluation of \mathcal{Q}_n reduces to solving two inverse problems for circular resistor networks, one for the reference conductivity, another for the unknown conductivity.

In this paper we extend the inversion approach introduced in [11, 49] to the case of partial boundary measurements. All the steps of the algorithm, except the essential one that defines the reconstruction mapping \mathcal{Q}_n , are independent of the distribution

of the measurement points on \mathcal{B} . They are therefore the same as in [11, 49], and we do not repeat them here. Our result is the construction of the optimal grids and thus of mapping Q_n for partial measurements.

The optimal grids for full boundary measurements are based on the rotational symmetry of the continuum problem for constant σ . They maintain the symmetry in the discrete setting, by being tensor product grids with uniform angular spacing. They are adaptive in the radial direction, with optimally placed radial nodes so that finite volume discretizations compute exactly the measurements[§] of the DtN map for constant σ . The grids have nice extrapolation properties, i.e. they give good approximations of the discrete measurements for a wide class of conductivities, and this is why we can use them in combination with the solution of discrete inverse problems for resistor networks to obtain the reconstruction mapping Q_n .

For partial boundary measurements there is no rotational symmetry in the problem, so it is not immediately clear what class of grids should we look for, and how to construct them so that they have good approximation properties in some class of conductivity functions. Our main result in this paper is that the grids can be constructed with an elegant approach based on extremal quasiconformal mappings [45] that transform the problem with partial measurements to a problem with full boundary measurements.

There are many transformations (diffeomorphisms) of the unit disk \mathbb{D} to itself that take the EIT problem with measurements of Λ_σ on \mathcal{B}_A to the EIT problem with measurements of $\Lambda_{\tilde{\sigma}}$ on \mathcal{B} . Here $\tilde{\sigma}$ is the transformed conductivity, and it is matrix valued (anisotropic), in general. Anisotropic conductivities are not uniquely recoverable from the DtN map [47], so our mappings should either preserve the isotropy of σ (i.e., be conformal) or, at least minimize its anisotropy (i.e., be extremal quasiconformal) [35]. In other words, we can obtain grids for partial boundary measurements that have good approximation properties for a class of conductivity functions, including constant ones, via extremal quasiconformal mappings of the optimal grids for full boundary measurements.

The paper is organized as follows: We begin in section 2 with a brief review of the inversion algorithm on optimal grids introduced in [11, 49] for the EIT problem with full boundary measurements. Then, we consider in section 3 conformal and quasiconformal coordinate transformations of the EIT problem with partial measurements, which we then use to obtain the numerical results in section 4. The conformal mappings are easy to compute (they are Möbius transforms) and they preserve the isotropy of the conductivity. However, as we show in section 3.2, they produce grids with a particular distribution of the measurement points in \mathcal{B}_A , and they are refined only near the center of \mathcal{B}_A . This leads to reconstructions with poor resolution away from the center of the accessible boundary. Our construction of the extremal quasiconformal (Teichmüller) mappings is based on their decomposition in terms of two conformal maps and an affine coordinate stretch [44], as described in section 3.3. The quasiconformal grids can be used for more general distributions of the measurement points in \mathcal{B}_A and they have better (more uniform) refinement properties, as shown in section 3.5. The algorithm for computing the reconstruction mapping Q_n is in section 4.1 and the details of its implementation are in section 4.2. The numerical results are in sections 4.3 and 4.4. We end in section 5 with a summary

[§] Here, by measurements we mean a measurement operator that takes Λ_σ to a discrete set of data at boundary points. See section 2.3.

and conclusions.

2. EIT with resistor networks

At the core of our inversion method is the solution of the discrete EIT problem of finding conductances of resistors in a network from discrete measurements of the DtN map. We begin in section 2.1 by motivating the resistor networks in the context of discretizing equation (1.1) with a finite volumes scheme. The inverse problem for resistor networks is stated in section 2.2, where we also review the existence and uniqueness of its solution. The connection between the continuum and discrete DtN maps is given in section 2.3. Then, we describe in section 2.4 the optimal grids, which are essential for obtaining an approximate solution of the continuum EIT problem from the solution of the discrete one. Finally, we conclude with some properties of the optimal grids in section 2.5.

Note that the optimal grids reviewed in this section apply to the case of full boundary measurements. The construction of the optimal grids for partial boundary measurements is the main result of this paper, and we give it in section 3.

2.1. Finite volume discretization and resistor networks

In finite volumes, we discretize equation (1.1) on a staggered grid consisting of interlacing primary and dual grid lines, which may be curvilinear. The potential u is discretized at the primary nodes, which are the intersections of the primary grid lines. The current fluxes $\sigma \nabla u$ are discretized at the dual nodes, where the dual grid lines intersect.

Let $P_{i,j}$ be a primary grid node in \mathbb{D} , as shown in figure 1, and integrate equation (1.1) over the dual grid cell $V_{i,j}$ with boundary $\partial V_{i,j}$ given by the union of four edges

$$\partial V_{i,j} = \Sigma_{i,j+\frac{1}{2}} \cup \Sigma_{i+\frac{1}{2},j} \cup \Sigma_{i,j-\frac{1}{2}} \cup \Sigma_{i-\frac{1}{2},j}. \quad (2.1)$$

Here $\Sigma_{i,j+\frac{1}{2}} = (P_{i-\frac{1}{2},j+\frac{1}{2}}, P_{i+\frac{1}{2},j+\frac{1}{2}})$ and the remaining edges are defined similarly. We obtain the balance of current fluxes across $\partial V_{i,j}$

$$\int_{V_{i,j}} \nabla \cdot (\sigma \nabla u) dV = \left(\int_{\Sigma_{i,j+\frac{1}{2}}} + \int_{\Sigma_{i+\frac{1}{2},j}} + \int_{\Sigma_{i,j-\frac{1}{2}}} + \int_{\Sigma_{i-\frac{1}{2},j}} \right) \sigma \frac{\partial u}{\partial \nu} d\Sigma = 0, \quad (2.2)$$

which we approximate with a one-point quadrature rule. For example, the first term in (2.2) becomes

$$\int_{\Sigma_{i,j+\frac{1}{2}}} \sigma \frac{\partial u}{\partial \nu} d\Sigma \approx \sigma(P_{i,j+\frac{1}{2}}) \frac{\partial u}{\partial \nu} \Big|_{P_{i,j+\frac{1}{2}}} L(P_{i+\frac{1}{2},j+\frac{1}{2}}, P_{i-\frac{1}{2},j+\frac{1}{2}}) \quad (2.3)$$

$$\approx \sigma(P_{i,j+\frac{1}{2}}) \frac{L(P_{i+\frac{1}{2},j+\frac{1}{2}}, P_{i-\frac{1}{2},j+\frac{1}{2}})}{L(P_{i,j+1}, P_{i,j})} (u(P_{i,j+1}) - u(P_{i,j})), \quad (2.4)$$

where $P_{i,j+\frac{1}{2}}$ is the intersection of the primary grid line $(P_{i,j}, P_{i,j+1})$ with $\Sigma_{i,j+\frac{1}{2}}$, and $L(P, Q)$ denotes the arc length between adjacent nodes P and Q along the primary and dual grid lines. The grid lines are assumed orthogonal in (2.4).

We obtain a linear system of difference equations for all $P_{i,j} \in \mathbb{D}$,

$$\begin{aligned} & \gamma_{i,j+\frac{1}{2}} (u_{i,j+1} - u_{i,j}) + \gamma_{i+\frac{1}{2},j} (u_{i+1,j} - u_{i,j}) + \\ & \gamma_{i,j-\frac{1}{2}} (u_{i,j-1} - u_{i,j}) + \gamma_{i-\frac{1}{2},j} (u_{i-1,j} - u_{i,j}) = 0, \end{aligned} \quad (2.5)$$

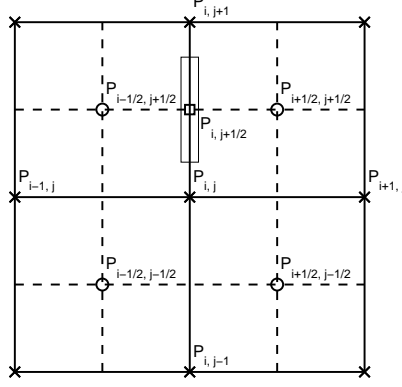


Figure 1. Finite volume discretization on a staggered tensor-product grid. Primary grid lines are solid, dual grid lines are dashed. Primary grid nodes are \times , dual grid nodes are \circ . Resistor is a white rectangle with a midpoint \square .

where we introduced the notation

$$\gamma_{i,j+\frac{1}{2}} = \sigma(P_{i,j+\frac{1}{2}}) \frac{L(P_{i+\frac{1}{2},j+\frac{1}{2}}, P_{i-\frac{1}{2},j+\frac{1}{2}})}{L(P_{i,j+1}, P_{i,j})}. \quad (2.6)$$

These equations can be interpreted as Kirchhoff's node law for a resistor network with topology determined by the primary grid. The nodes of the network are the primary grid nodes and the primary grid lines are the network edges with conductances $\gamma_{\alpha,\beta} > 0$, where α, β are indices of the edges.

Note that since for $\sigma \equiv 1$ we have

$$\gamma_{i,j+\frac{1}{2}}^{(1)} = \frac{L(P_{i+\frac{1}{2},j+\frac{1}{2}}, P_{i-\frac{1}{2},j+\frac{1}{2}})}{L(P_{i,j+1}, P_{i,j})}, \quad (2.7)$$

we can rewrite (2.6) as

$$\gamma_{i,j+\frac{1}{2}} = \sigma(P_{i,j+\frac{1}{2}}) \gamma_{i,j+\frac{1}{2}}^{(1)}. \quad (2.8)$$

We use this observation in section 2.4, where we introduce the optimal grid.

2.2. The discrete EIT problem

Similar to the continuum case, we can define the DtN map of a network. We begin with some notation. Let $\Gamma = (V, E)$ be the planar graph of the resistor network. The set of nodes V is the union of two disjoint sets B and I , and E is the set of edges connecting the nodes in V . We are interested in circular planar graphs, with Γ embedded in the unit disk \mathbb{D} . The embedding is such that the nodes in I lie strictly inside the unit disk and the nodes in B lie on the unit circle $\mathcal{B} = \partial\mathbb{D}$. Therefore, we call I the set of interior nodes, and B the set of boundary nodes.

Let $u : V \rightarrow \mathbb{R}$ be a potential function. We denote its restriction to the interior nodes by u_I and to the boundary nodes by u_B . Let also $\gamma : E \rightarrow \mathbb{R}^+$ be a conductance function that assigns a positive conductance $\gamma(e)$ to each edge $e \in E$. The potential satisfies Kirchhoff's node law (2.5) at all the interior nodes. The boundary conditions

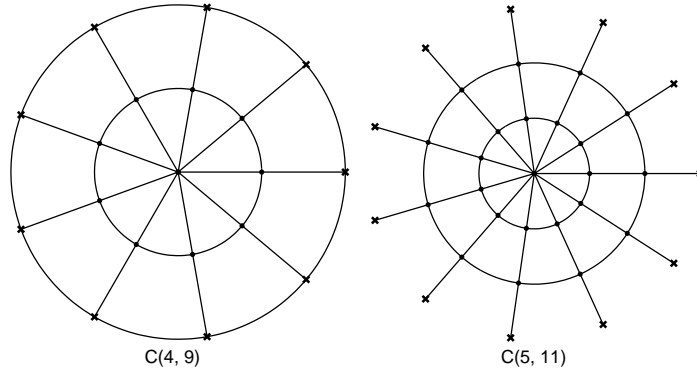


Figure 2. Circular resistor networks $C(l, n)$ with critical graphs: $l = (n-1)/2$. Interior nodes given as dots, boundary nodes as crosses.

u_B can be set arbitrarily, and the resulting boundary currents are denoted by J_B . The DtN map of the network is the linear operator with matrix $\Lambda_\gamma \in \mathbb{R}^{n \times n}$, such that

$$\Lambda_\gamma u_B = J_B. \quad (2.9)$$

Here n is the cardinality of B ($n = |B|$).

The discrete EIT problem is to determine the function γ from the DtN map Λ_γ . It has been shown in [15] that the problem is uniquely solvable for networks with *critical* graphs, whose definition we now recall.

Let $\pi(\Gamma)$ be the set of all circular pairs connected through Γ by disjoint paths. A circular pair (P, Q) consists of two subsets of boundary nodes P and Q , of equal cardinality $|P| = |Q| = k$, such that the nodes in P and Q lie on two disjoint arcs of \mathcal{B} . The nodes are ordered according to the orientation of \mathcal{B} . This order is called circular. The circular pair is said to be *connected* if there exist k disjoint paths in Γ connecting the nodes in P and Q .

Definition 1. *The graph Γ is called critical, if removing any edge breaks some connection in $\pi(\Gamma)$.*

Following [11, 49] we consider in this paper networks with a special topology, as illustrated in figure 2. These networks are called in [14] *circular resistor networks*, and are denoted by $C(l, n)$. The notation indicates that the network has l layers and n resistors in each layer. These resistors may be aligned along the radius (radial resistors), or they may be transversal to the radius (angular resistors). The layers of radial and angular resistors alternate, with the innermost layer being radial. It is shown in [11, 49] that the graph of $C(l, n)$ is critical if and only if n is odd and $l = (n-1)/2$. This is why we consider in this paper circular resistor networks of the form $C((n-1)/2, n)$, with odd n .

The discrete EIT problem for networks $C(l, n)$ can be solved with at least two approaches. The first approach is a direct layer peeling method [14] which solves the nonlinear EIT problem in a finite number of algebraic operations. It begins by determining the conductances in the outermost layer adjacent to the boundary nodes. Then it peels off the layer and proceeds inwards. The algorithm stops when the innermost layer of resistors is reached. The advantage of layer peeling is that it is fast

and explicit. The disadvantage is that it quickly becomes unstable, as the number of layers grows. The second approach is to solve the discrete EIT problem with non-linear, regularized least squares, as in [9]. In general, it is unclear how to regularize the least squares for network recovery using penalty terms, because we cannot speak of regularity assumptions (such as total variation) in the discrete setting. We have recovered in [9] networks with optimization using a Gauss-Newton iteration regularized with the SVD truncation of the Jacobian. Adaptive SVD truncation of the Jacobian allows the Gauss-Newton iteration to converge without the use of artificial penalty terms. The advantage of optimization is that in general it allows the recovery of larger networks than layer peeling. The downside is the increased computational cost. All the computations in this paper use the layer peeling algorithm from [14].

2.3. The measurements of the continuum DtN map as a discrete DtN map

To connect the continuum EIT problem with the discrete one for circular networks, we first define the discrete DtN map Λ_γ in terms of the continuum one Λ_σ , using a measurement operator \mathcal{M}_n ,

$$\Lambda_\gamma = \mathcal{M}_n(\Lambda_\sigma). \quad (2.10)$$

In the simplest case considered in [14, 28], \mathcal{M}_n takes point values of Λ_σ . Here we describe the more general measurement operator introduced [11, 49], which lumps fluxes over disjoint segments (electrode supports) \parallel of the boundary.

Let χ_1, \dots, χ_n be nonnegative functions in $H^{1/2}(\mathcal{B})$, with disjoint supports, numbered in circular order on \mathcal{B} . These functions are normalized by

$$\int_0^{2\pi} \chi_j(\theta) d\theta = 1, \quad j = 1, \dots, n, \quad (2.11)$$

and we can interpret them as models of the electrode supports. The operator \mathcal{M}_n maps Λ_σ to the symmetric $n \times n$ matrix Λ_γ , with off-diagonal entries given by

$$(\Lambda_\gamma)_{i,j} = (\mathcal{M}_n(\Lambda_\sigma))_{i,j} = \langle \chi_i, \Lambda_\sigma \chi_j \rangle, \quad i \neq j, \quad (2.12)$$

where $\langle \cdot, \cdot \rangle$ is the duality pairing between $H^{1/2}(\mathcal{B})$ and $H^{-1/2}(\mathcal{B})$. The diagonal entries of Λ_γ are determined by the conservation of currents

$$(\Lambda_\gamma)_{i,i} = (\mathcal{M}_n(\Lambda_\sigma))_{i,i} = - \sum_{j \neq i} (\mathcal{M}_n(\Lambda_\sigma))_{i,j}, \quad i = 1, \dots, n. \quad (2.13)$$

It follows from [11, 49] that $\mathcal{M}_n(\Lambda_\sigma)$ is a DtN map of a circular resistor network with critical graph. This is shown in [11, 49] using the complete characterization of the set \mathcal{D}_n of DtN maps of circular resistor networks with critical graphs given in [15, 14, 18] and the characterization of the kernel of the continuum DtN map in [30].

Thus, the measurements $\mathcal{M}_n(\Lambda_\sigma)$ are consistent with a unique resistor network $C((n-1)/2, n)$, with odd number n of boundary nodes and conductance γ . This is not sufficient however to obtain an approximate solution of the continuum EIT problem. We observe from relation (2.8) that in order to estimate $\sigma(P_{\alpha,\beta})$ we need $\gamma_{\alpha,\beta}^{(1)}$, as well as the points $P_{\alpha,\beta}$ of intersection of the grid lines. Thus, to obtain an approximate

\parallel Other measurement operators that use more accurate electrode models, such as the ‘‘complete electrode’’ model can be used in principle. The extension of the theory to such models requires a proof of consistency of such measurements with the DtN maps of critical circular resistor networks, the analogue of Theorem 1 in [11]. If such consistency holds, the solution of the discrete inverse problem is obtained the same way as with the operator \mathcal{M}_n considered here.

solution to the continuum inverse problem we must know the discretization grid. We describe next the approach in [11, 49] that approximates the conductivity on *optimal grids*.

2.4. From the discrete inversion to continuum: the optimal grids

We now review briefly the results in [11, 49], which use optimal grids to solve the EIT problem with full boundary measurements. The optimal grids are defined in [11, 49] as the grids given by (2.7), in terms of the conductances $\gamma_{\alpha,\beta}^{(1)}$ of the network $C((n-1)/2, n)$ with the measured DtN map corresponding to the constant conductivity

$$\Lambda_{\gamma^{(1)}} = \mathcal{M}_n(\Lambda_1), \quad (2.14)$$

where Λ_1 is the continuum DtN map for $\sigma \equiv 1$. That is, the term optimal refers to the fact that the finite volume discretization on these grids gives the exact DtN map (2.14).

The continuum EIT problem with full boundary measurements has the important property of rotational invariance for layered conductivities $\sigma(r, \theta) = \sigma(r)$, which of course includes the case $\sigma \equiv 1$. To maintain this rotational invariance in the discrete setting, the measurements of the DtN map are centered at equidistant points on \mathcal{B} . Explicitly, the measurement functions $\chi_j(\theta)$ are angular translations of the same function χ ,

$$\chi_k(\theta) = \chi(\theta - \theta_k), \quad (2.15)$$

such that $\text{supp}\chi \subset (\hat{\theta}_0, \hat{\theta}_1)$, where $\theta_k = 2\pi(k-1)/n$ and $\hat{\theta}_k = 2\pi(k-1/2)/n$ are the primary and dual boundary grid nodes respectively, for $k = 1, \dots, n$.

Then, the problem simplifies for layered conductivities, because when taking Fourier transforms in θ , the problem becomes one dimensional. The same simplification can be made in the discrete setting, by taking the discrete Fourier transform, provided that we have a tensor product discretization grid with the boundary nodes given above. The placement of the radial nodes in this tensor product grid is obtained as we describe below.

Let us introduce an integer parameter m and a binary $m_{1/2} \in \{0, 1\}$, such that the number of layers is $l = 2m + m_{1/2} + 1$, where $m_{1/2}$ determines if the outer layer in $C(l, n)$ is radial ($m_{1/2} = 0$) or circular ($m_{1/2} = 1$). The grid is staggered and the primary radii r_j and the dual radii \hat{r}_j are ordered as

$$1 = r_1 = \hat{r}_1 > r_2 > \hat{r}_2 > \dots > r_{m+1} > \hat{r}_{m+1} > r_{m+2} > 0, \quad \text{for } m_{1/2} = 0, \quad (2.16)$$

$$1 = \hat{r}_1 = r_1 > \hat{r}_2 > r_2 > \dots > r_{m+1} > \hat{r}_{m+2} > r_{m+2} > 0, \quad \text{for } m_{1/2} = 1. \quad (2.17)$$

To determine these radii, we must solve a discrete EIT problem to get $\gamma^{(1)}$ from (2.14). The method of solution is similar to that of finding γ from (2.10). In our numerical computations we determine $\gamma^{(1)}$ and γ with the layer peeling algorithm described in [14].

Consistent with the notation in (2.16) and (2.17), we denote by $\gamma_{j,k}$ the conductances of radial resistors and by $\hat{\gamma}_{j,k}$ the conductances of the angular resistors. The formulas (2.6) become

$$\gamma_{j,k} = \sigma(\hat{r}_{j+m_{1/2}}, \theta_k) \frac{\hat{r}_{j+m_{1/2}} h_\theta}{r_j - r_{j+1}}, \quad j = 1, \dots, m+1, \quad k = 1, \dots, n, \quad (2.18)$$

$$\hat{\gamma}_{j,k} = \sigma(r_j, \hat{\theta}_k) \frac{\hat{r}_{j+m_{1/2}-1} - \hat{r}_{j+m_{1/2}}}{r_j h_\theta}, \quad j = 2 - m_{1/2}, \dots, m+1, \quad k = 1, \dots, n, \quad (2.19)$$

where $h_\theta = 2\pi/n$ is the angular grid step. We refer to these equations as the *averaging formulas*.

Since the family of measurement functions $\chi_k(\theta)$ is chosen to be rotationally invariant, the matrix $\mathcal{M}_n(\Lambda_1)$ is circulant. Thus, in the case $\sigma \equiv 1$, the solution $\gamma_{j,k}^{(1)}$, $\widehat{\gamma}_{j,k}^{(1)}$ of (2.14) does not depend on the angular index k , and the resulting optimal grid is indeed a tensor product grid. Once the conductances $\gamma_j^{(1)}$, $\widehat{\gamma}_j^{(1)}$ are known, the radii of the optimal grid are obtained sequentially from equations (2.18)–(2.19), starting at the boundary with $r_1 = \widehat{r}_1 = 1$. We obtain

$$r_{j+1} = r_j - h_\theta \widehat{r}_{j+m_{1/2}} / \gamma_j^{(1)}, \quad j = 1, \dots, m+1, \quad (2.20)$$

$$\widehat{r}_{j+1} = \widehat{r}_j - h_\theta r_{j+1-m_{1/2}} \widehat{\gamma}_{j+1-m_{1/2}}^{(1)}, \quad j = 1, \dots, m+m_{1/2} \quad (2.21)$$

The main result in [11, 49] is that the optimal grid (2.20)–(2.21) can be used to find an approximate solution of the continuum EIT problem. Explicitly, the grid is used in [11, 49] to define a nonlinear mapping $\mathcal{Q}_n : \mathcal{D}_n \rightarrow \mathcal{S}$ from the discrete data $\Lambda_\gamma \in \mathcal{D}_n$ to the space \mathcal{S} of positive and bounded conductivities. Depending on the smoothness of the unknown conductivity, this mapping is an approximate inverse of the forward map

$$\mathcal{F}_n : \mathcal{S} \rightarrow \mathcal{D}_n, \quad \mathcal{F}_n(\sigma) = \mathcal{M}_n(\Lambda_\sigma) \in \mathcal{D}_n.$$

It acts therefore as a preconditioner of \mathcal{F}_n , for a Newton type iteration that seeks an approximate solution of the continuum EIT problem.

The map \mathcal{Q}_n is defined as follows. First, we compute the solution $\gamma_{\alpha,\beta}$ of the discrete inverse problem (2.10) with data $\Lambda_\gamma = \mathcal{M}_n(\Lambda_\sigma)$. Then, we estimate from (2.8) the values of the unknown conductivity at the intersections $P_{\alpha,\beta}$ of the primary and dual grid lines

$$\sigma(P_{\alpha,\beta}) \approx \frac{\gamma_{\alpha,\beta}}{\gamma_{\alpha,\beta}^{(1)}}. \quad (2.22)$$

The map $\mathcal{Q}_n(\Lambda_\gamma)$ returns the interpolation (linear) in \mathbb{D} of the values (2.22) at the optimal grid nodes $P_{\alpha,\beta}$. We refer to $\mathcal{Q}_n(\Lambda_\gamma)$ as the *reconstruction*. It can be improved further, with an iterative scheme, as described in [11, 49].

Note that the averaging formulas (2.18)–(2.19) correspond to the discretization of the forward problem. However, we use them for the conductances $\gamma_{j,k}$ and $\widehat{\gamma}_{j,k}$ that solve the discrete inverse problem. These conductances are not the same as in the forward problem, unless we use a grid that makes the averaging formulas exact. The results in [11, 49] show that the optimal grids that make the averaging formulas exact in the case $\sigma \equiv 1$, also give a good approximation for a wider class of conductivities. This is the justification of approximation (2.22).

Note also that formulas (2.18)–(2.19) and (2.20)–(2.21) are not the only possible relations that can be used to determine the grid from the solution $\gamma_j^{(1)}$, $\widehat{\gamma}_j^{(1)}$ of (2.14). In fact a different set of relations was used in [11, 49]. We refer to these relations as log-averaging, and give their definition in Appendix A.

Finally, there are alternative choices of the measurement operator. In particular, in the case of layered conductivities, there exists a measurement operator \mathcal{M}_n^* , that leads to an explicit solution of the discrete EIT problem [5], which can then be used to prove certain properties of the optimal grids. This is done in detail in Appendix A.

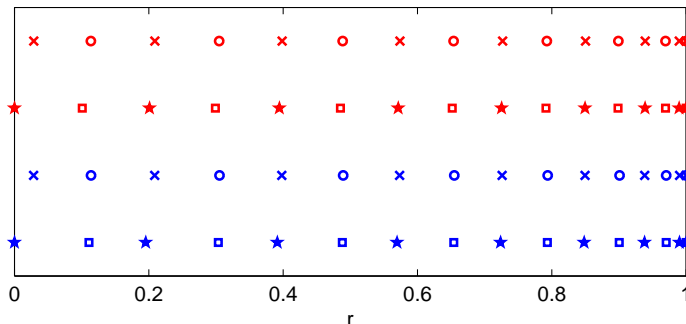


Figure 3. Radial optimal grids for different choices of averaging formulas and measurement operators ($n = 31$). Top two grids (red) correspond to $\mathcal{M}_n^*(\Lambda_1)$, bottom two grids (blue) correspond to $\mathcal{M}_n(\Lambda_1)$. Log-averaging formulas: primary \times , dual \circ . Averaging formulas (2.20)–(2.21): primary \star , dual \square .

2.5. Properties of optimal grids

We show in figure 3 the radial optimal grids corresponding to the measurement operators $\mathcal{M}_n(\Lambda_1)$ and $\mathcal{M}_n^*(\Lambda_1)$ and two choices of averaging formulas: The formulas (2.18)–(2.19) and the log-averaging formulas used in [11, 49] and described in Appendix A. We observe that the grids obtained from the same averaging formulas but different measurement operators are almost indistinguishable. There is a slight difference between the grids given by the two averaging formulas, but this difference is mostly near the origin $r = 0$. We have observed from extensive numerical experiments, for a variety of grid sizes, that the optimal grids are robust with respect to the choice of measurement operator and averaging formulas.

The grids presented in figure 3 share two common properties. First, they are indeed staggered with interlacing primary and dual nodes. Second, they are refined near the boundary of the unit disk $r = 1$, where the DtN map is measured. The gradual refinement towards the boundary accounts for the loss of resolution of the EIT problem inside the domain. These properties were observed in numerical experiments in [11, 49]. We prove them in Appendix A, using the results of [5].

3. Coordinate transformations and the EIT

Our main result in this paper is the extension of the reconstruction mapping $\mathcal{Q}_n(\Lambda_\gamma)$ to the case of partial boundary measurements. The other steps in the inversion method are the same as in the full boundary measurement case, and they are presented in detail in [11, 49]. This is why we do not repeat them here, and we focus our attention solely on $\mathcal{Q}_n(\Lambda_\gamma)$, for Λ_γ measured on the accessible boundary $\mathcal{B}_A \subset \mathcal{B}$.

The key idea is to map the partial data discrete EIT problem to the problem with measurements at equidistant points all around the boundary, where we already know how to define the optimal grids. Both problems are solved in \mathbb{D} , so we consider diffeomorphisms of the unit disk to itself.

Denote such a diffeomorphism by F and its inverse by G . If u solves (1.1), then

$\tilde{u}(x) = u(F(x))$ satisfies a similar equation with conductivity $\tilde{\sigma}$ given by

$$\tilde{\sigma}(x) = \frac{G'(y)\sigma(y)(G'(y))^T}{|\det G'(y)|} \Big|_{y=F(x)}, \quad (3.1)$$

where G' denotes the Jacobian of G . The conductivity $\tilde{\sigma}$ in (3.1) is the *push forward* of σ by G , and it is denoted by $G_*(\sigma)$. Note that if $G'(y)(G'(y))^T \neq I$, then $\tilde{\sigma}$ is a symmetric positive definite tensor provided $\det G'(y) \neq 0$. Thus, in general the push forward of an isotropic conductivity is anisotropic.

To write the transformed DtN map, we use the restrictions of diffeomorphisms G and F to the boundary $g = G|_{\mathcal{B}}$ and $f = F|_{\mathcal{B}}$. Then, the push forward of the DtN map $g_*\Lambda_\sigma$ is

$$((g_*\Lambda_\sigma)\psi)(\theta) = (\Lambda_\sigma(\psi \circ g))(\tau)|_{\tau=f(\theta)}, \quad \theta \in [0, 2\pi), \quad (3.2)$$

for $\psi \in H^{1/2}(\mathcal{B})$. As shown in [47], the DtN map is invariant under the push forward in the following sense

$$g_*\Lambda_\sigma = \Lambda_{G_*\sigma}. \quad (3.3)$$

This invariance tells us that given a diffeomorphism F , its boundary restriction $f = F|_{\mathcal{B}}$, their respective inverses G and g , and the DtN map Λ_σ , we can compute the push forward of the DtN map, solve the inverse problem for $g_*\Lambda_\sigma$ to obtain $\tilde{\sigma}$, and then map it back using the inverse of (3.2). We will use the discrete analogue of this fact to transform the discrete measurements Λ_γ of Λ_σ on \mathcal{B}_A to discrete measurements at the equidistant points θ_k , from which we can estimate $\tilde{\sigma}$ with the method described in section 2.4.

Note however that the EIT problem is uniquely solvable only for isotropic conductivities. Anisotropic conductivities can be determined from the DtN map only up to a boundary-preserving diffeomorphism [47]. To overcome this ambiguity we propose two distinct approaches described in the next sections. The first approach is based on conformal mappings, which preserve the isotropy of the conductivity, at the expense of rigid placement of the measurement points in \mathcal{B}_A . The second approach uses extremal quasiconformal mappings, that minimize the artificial anisotropy of the reconstructed conductivity introduced by a general placement of the boundary measurement points in \mathcal{B}_A .

3.1. Conformal mappings and inversion grids

To ensure that the push forward (3.1) of the isotropic σ is isotropic itself, the mapping must satisfy $G'((G')^T) = I$ or, equivalently, $F'((F')^T) = I$. It means that F is *conformal* and the resulting conductivity is

$$G_*(\sigma) = \sigma \circ F. \quad (3.4)$$

Since all conformal mappings of the unit disk to itself belong to the family of Möbius transforms [36], F must be of the form

$$F(z) = e^{i\omega} \frac{z - a}{1 - \bar{a}z}, \quad z \in \mathbb{D}, \quad \omega \in [0, 2\pi), \quad a \in \mathbb{C}, \quad |a| < 1, \quad (3.5)$$

where we associate \mathbb{R}^2 with the complex plane \mathbb{C} .

It remains to determine the constant parameters ω and a in (3.5). Let the accessible boundary \mathcal{B}_A be the circular segment

$$\mathcal{B}_A = \{e^{i\tau} \mid \tau \in [-\beta, \beta]\}, \quad (3.6)$$

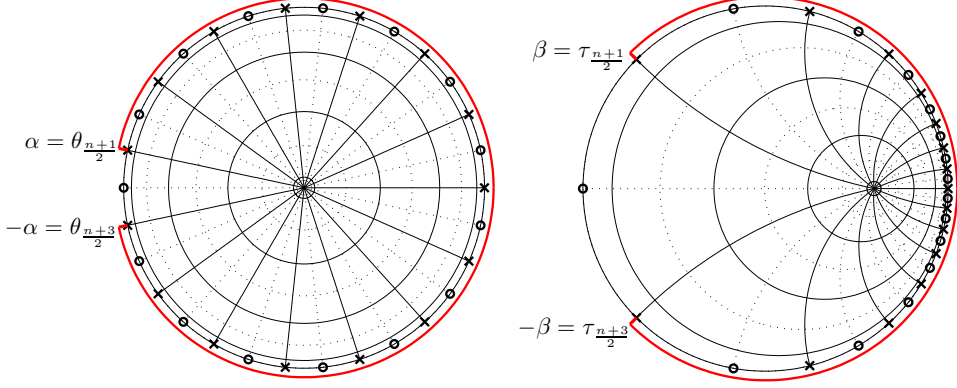


Figure 4. The optimal grid with $n = 15$ under the conformal mapping F , with $\beta = 3\pi/4$. Left: the optimal grid; right: the image of the optimal grid under F . Primary grid lines are solid black, dual grid lines are dotted black. Boundary grid nodes: primary \times , dual \circ . Accessible boundary is solid red.

with $\beta \in (0, \pi)$. The inaccessible boundary is $\mathcal{B}_I = \mathcal{B} \setminus \mathcal{B}_A$. The restriction of (3.5) to \mathcal{B} is denoted by

$$f(\theta) = F(e^{i\theta}). \quad (3.7)$$

It maps the boundary grid nodes $\theta_k, \widehat{\theta}_k$ defined in section 2.4 to the transformed grid nodes $\tau_k, \widehat{\tau}_k$ in \mathcal{B}_A , for $k = 1, \dots, n$. We assume point-like measurements (2.15) (χ_k have very small support), so that we can map any primary interval (θ_k, θ_{k+1}) to \mathcal{B}_I . Specifically, we take the interval $(\theta_{(n+1)/2}, \theta_{(n+3)/2})$ shown in figure 4. Let $\alpha = \pi(1 - 1/n)$, then the condition

$$f((\theta_{(n+1)/2}, \theta_{(n+3)/2})) = \mathcal{B}_I \quad (3.8)$$

becomes $F(e^{\pm i\alpha}) = e^{\pm i\beta}$ and the parameters of the Möbius transform are

$$a = \frac{\cos \alpha - \cos \beta}{1 - \cos(\alpha + \beta)}, \quad \omega = 0. \quad (3.9)$$

We show in figure 4 the transformation \mathfrak{N} of the optimal grid, which we name the *conformal mapping grid*. Note that by enforcing the condition (3.8), we have exhausted all degrees of freedom of the Möbius transform, and thus, we have no control over the placement of the boundary grid nodes $\tau_k, \widehat{\tau}_k$. The resulting grid is refined towards the middle of the accessible boundary, and it is very sparse near the inaccessible boundary. This behavior persists as we increase the number n of primary boundary points, as we now explain.

3.2. The limit distribution of boundary nodes in conformal mapping grids

To describe the asymptotic distribution of the boundary nodes under the conformal mappings, it is convenient to renumber $\tau_k, \widehat{\tau}_k$. We define $\widetilde{\tau}_l = f(\pi + l\pi/n)$,

\mathfrak{N} The grid is obtained with the log-averaging formulas and the \mathcal{M}_n^* measurements described in Appendix A.

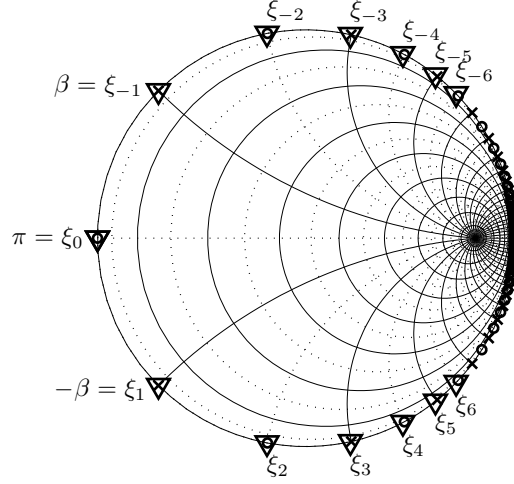


Figure 5. Limiting behavior ($n = 37$) of the image of the optimal grid under F , with $\beta = 3\pi/4$. Primary grid lines are solid, dual grid lines are dotted. Boundary grid nodes: primary τ_k are \times , dual $\hat{\tau}_k$ are \circ . Limiting nodes $\xi_l = \lim_{n \rightarrow \infty} \tilde{\tau}_l$ for $l = -6, \dots, 6$ are ∇ .

$l = -n + 1, \dots, n$, so that when l is odd, $\tilde{\tau}_l$ is a primary node and when l is even, it is a dual node. Then, we obtain after substituting (3.9) in (3.5), that

$$\cos \xi_l = \lim_{n \rightarrow \infty} \cos \tilde{\tau}_l = \frac{l^2 - 1 + (l^2 + 1) \cos \beta}{l^2 + 1 + (l^2 - 1) \cos \beta}, \quad (3.10)$$

$$\sin \xi_l = \lim_{n \rightarrow \infty} \sin \tilde{\tau}_l = \frac{2l \sin \beta}{l^2 + 1 + (l^2 - 1) \cos \beta}. \quad (3.11)$$

This limit distribution has a unique accumulation point at $\tau = 0$, as $l \rightarrow \infty$.

We illustrate the asymptotic behavior of the grid in figure 5. We observe that already for $n = 37$ the leftmost 13 nodes $\tilde{\tau}_l$ are very close to their limit values ξ_l , $l = -6, \dots, 6$. That is, as we increase n , there will be no further angular refinement of the grid in that region.

Note that as $n \rightarrow \infty$ and therefore $\alpha \rightarrow \pi$, the parameter a defined by (3.9) tends to -1 . Thus, the pole $1/\bar{a}$ of the Möbius transform (3.5) approaches $-1 \in \mathcal{B}$, and the mapping F degenerates in \mathbb{D} .

The limiting behavior of the optimal grid under conformal automorphisms of \mathbb{D} may suggest that the conformal mapping approach is not useful for solving the partial data EIT problem. After all, it is natural to expect the inversion grid to provide a converging scheme for the solution of the forward problem, for which grid refinement is a necessary condition. However, the instability of the EIT problem implies that we cannot improve the resolution of the reconstructions by simply taking more measurement points. Put otherwise, the limit $n \rightarrow \infty$ is not practically important in this problem. The numerical results in section 4 demonstrate that the conformal mapping approach gives reasonable reconstructions of the conductivity σ .

3.3. Quasiconformal mappings and anisotropy

So far we have identified two features of the conformal mapping grids, that may present problems for inversion. First, once the number of boundary grid nodes n and the size of the inaccessible boundary are fixed, we have no control over the positioning of the boundary grid nodes τ_k , where the measurements are made. Second, the grid does not refine asymptotically as $n \rightarrow \infty$. This is because the group of conformal automorphisms of the unit disk is too rigid. A more general approach would be to use a richer family of transforms at a price of introducing some anisotropy in the reconstruction. A suitable family of mappings that allows the control of the artificial anisotropy of the reconstruction consists of *quasiconformal* mappings.

A quasiconformal mapping $W(z)$ is defined as a diffeomorphism that obeys the *Beltrami equation*

$$\frac{\partial W}{\partial \bar{z}} = \mu(z) \frac{\partial W}{\partial z}, \quad (3.12)$$

where the Beltrami coefficient $\mu(z)$ is a complex valued measurable function satisfying

$$\|\mu\|_\infty = \text{ess sup} |\mu(z)| < 1. \quad (3.13)$$

The Beltrami coefficient, also known as the *complex dilatation* $\mu(z)$ provides a measure of how much the mapping W differs from a conformal one. A conformal mapping corresponds to $\mu(z) \equiv 0$, in which case (3.12) reduces to the Cauchy-Riemann equation. In this paper we consider quasiconformal self mappings of the unit disk, so (3.12) and (3.13) hold for $z \in \mathbb{D}$.

Now let us describe the connection between the dilatation of the quasiconformal mapping and the anisotropy of the push-forward of an isotropic conductivity. Let $\tilde{\sigma}(z)$ be an anisotropic conductivity with eigenvalues $\lambda_1(z) \geq \lambda_2(z) > 0$. Its *anisotropy* at z is defined by

$$\kappa(\tilde{\sigma}, z) = \frac{\sqrt{L(z)} - 1}{\sqrt{L(z)} + 1}, \quad (3.14)$$

where $L(z) = \lambda_1(z)/\lambda_2(z)$, and

$$\kappa(\tilde{\sigma}) = \sup_z \kappa(\tilde{\sigma}, z) \quad (3.15)$$

is the maximum anisotropy. It is easy to show that the anisotropy of the push forward of an isotropic conductivity σ by a quasiconformal mapping W satisfies

$$\kappa(W_*(\sigma), z) = |\mu(z)|. \quad (3.16)$$

Thus, the L^∞ norm of the dilatation gives us a measure of the maximum anisotropy introduced by W to an isotropic conductivity

$$\kappa(W_*(\sigma)) = \|\mu\|_\infty. \quad (3.17)$$

Since the true unknown conductivity is isotropic, we would like to minimize the amount of anisotropy introduced into the reconstruction by the mapping W . This leads us to the *extremal* quasiconformal mappings, which minimize the maximum anisotropy $\|\mu\|_\infty$ under some constraints. In our case the constraints come in the form of prescribing the boundary value $f = W|_{\mathcal{B}}$, which gives us control over the positioning of the measurement points $\tau_k = f(\theta_k)$.

3.4. Extremal quasiconformal mappings

It is known [45] that for sufficiently regular boundary values f , there exists a unique extremal quasiconformal mapping that is a Teichmüller mapping, i.e. its Beltrami coefficient satisfies

$$\mu(z) = \|\mu\|_\infty \frac{\overline{\phi(z)}}{|\phi(z)|}, \quad (3.18)$$

for some holomorphic function $\phi(z)$ in \mathbb{D} . Using this in (3.16), we obtain that the push forward of an isotropic conductivity by a Teichmüller mapping has a uniform anisotropy throughout \mathbb{D} .

Similar to (3.18), we can define the dilatation of W^{-1} in terms of a holomorphic function ψ . Then, according to [43], we can decompose a Teichmüller mapping W into

$$W = \Psi^{-1} \circ A_K \circ \Phi, \quad (3.19)$$

where

$$\Phi(z) = \int \sqrt{\phi(z)} dz, \quad \Psi(\zeta) = \int \sqrt{\psi(\zeta)} d\zeta, \quad (3.20)$$

and A_K is affine. The mappings Φ and Ψ are conformal away from zeros of ϕ and ψ respectively. The only source of anisotropy in decomposition (3.19) is the affine mapping A_K , that we take to be

$$A_K(x + iy) = Kx + iy, \quad x, y \in \mathbb{R}, \quad (3.21)$$

where the constant parameter $K > 0$ determines the anisotropy

$$\kappa(W_*(\sigma)) = \|\mu\|_\infty = \left| \frac{K-1}{K+1} \right|. \quad (3.22)$$

To obtain the terms Φ and Ψ in the decomposition (3.19) of the Teichmüller mapping, we use the constraints on the boundary values $f = W|_{\mathcal{B}}$. Since we work with point-like boundary measurements, it is only important to have control over the behavior of the Teichmüller mapping at the measurement points $e^{i\theta_k}$. This leads us to consider the extremal polygonal quasiconformal mappings. A *polygon* in this context is a unit disk \mathbb{D} with n distinguished points on \mathcal{B} , called the *vertices* of the polygon (in our case $e^{i\theta_k}$).

The extremal polygonal quasiconformal mapping W takes the boundary points $e^{i\theta_k}$ to prescribed points $e^{i\tau_k}$, while minimizing the maximum dilatation. According to [46], the integrals Φ and Ψ in its decomposition map the unit disk conformally onto polygons comprised of a number of rectangular strips. But conformal mappings of the unit disk to polygons are Schwartz-Christoffel mappings [20], given by the general formula

$$S(z) = A + B \int^z \prod_{q=1}^N \left(1 - \frac{\zeta}{z_q}\right)^{\alpha_q - 1} d\zeta, \quad (3.23)$$

where $A, B \in \mathbb{C}$ are constants, N is the number of vertices of a polygon, $z_q \in \mathcal{B}$ are the pre-images of the vertices and α_q are the interior angles of the polygon. Moreover, for the polygons comprised of rectangular strips $\alpha_q \in \{1/2, 3/2\}$.

Comparing the definitions (3.20) of Φ and Ψ with (3.23) we observe that ϕ and ψ are rational functions with first order poles at vertices with angle $\pi/2$ and first order zeros at vertices with angle $3\pi/2$. This behavior is illustrated in detail in figure 6,

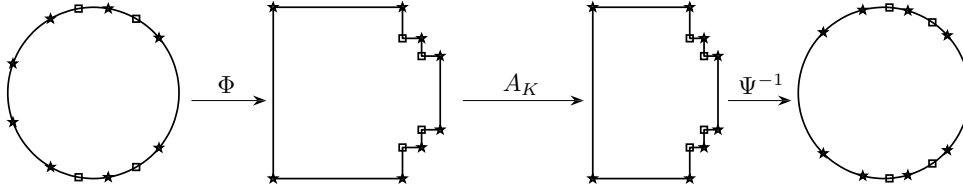


Figure 6. Teichmüller mapping decomposed into conformal mappings Φ and Ψ , and an affine transform A_K , $K = 3/4$. The poles of ϕ and ψ and their images under Φ and Ψ are \star , the zeros of ϕ and ψ and their images under Φ and Ψ are \square .

along with the behavior of each mapping in the decomposition (3.19). Note that we construct the mappings Φ , Ψ so that they are symmetric with respect to the real axis. This is done to maintain the symmetry of the optimal grid under W .

We have established that in order to map the unit disk to a polygon comprised of several rectangular strips it is necessary for ϕ and ψ to have zeros and poles on \mathcal{B} . In what follows we construct ϕ and ψ so that the zeros are at the dual grid nodes and the poles are at the primary grid nodes. Such construction gives us an extremal mapping, since according to [43], every Teichmüller mapping of the form (3.19) is extremal for the boundary values that it induces.

3.5. Teichmüller mappings and inversion grids

We illustrate the behavior of the optimal grids under the extremal quasiconformal mappings in figure 7. The number n of boundary primary grid nodes and the size of the accessible boundary are the same as for the conformal mapping example in figure 4, so that we can compare the two approaches. Similar to the conformal mapping case, we map the primary boundary grid interval $(\theta_{(n+1)/2}, \theta_{(n+3)/2})$ to the inaccessible boundary.

The grids for two different values of the affine stretching constant K are presented in figure 7, with the larger value of K corresponding to less artificial anisotropy. For $K = 0.8$ we already observe that the clustering of the boundary grid nodes around 1 is much less pronounced than for the conformal mapping grid. As we decrease K to 0.66 the grid nodes move further away from the middle of \mathcal{B}_A towards the inaccessible boundary. One should keep in mind that although the distribution of the grid nodes becomes more uniform for smaller values of K , the conductivity reconstructed on such grid would have a larger amount of artificial anisotropy, as shown in the numerical examples in the next section.

4. Numerical results

In this section we present numerical results for the reconstructions of smooth and piecewise constant conductivities. We begin in section 4.1 with the outline of the inversion method. Then, we describe our numerical implementation of the inversion method in section 4.2. The numerical results are in sections 4.3 and 4.4.

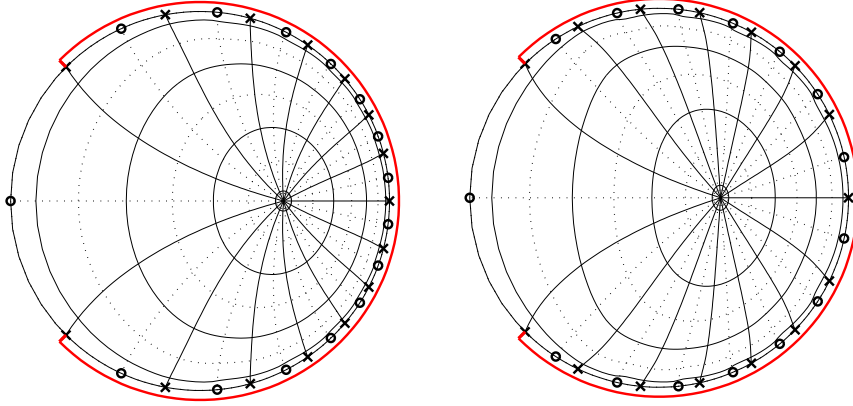


Figure 7. The optimal grid with $n = 15$ under the quasiconformal Teichmüller mappings W with different K . Left: $K = 0.8$; right: $K = 0.66$. Primary grid lines are solid black, dual grid lines are dotted black. Boundary grid nodes: primary \times , dual \circ . Accessible boundary is solid red.

4.1. The inversion method

What we mean by inversion method, is the computation of the reconstruction $\mathcal{Q}_n(\Lambda_\gamma)$ from the discrete measurements $\Lambda_\gamma = \mathcal{M}_n(\Lambda_\sigma)$ made at the accessible boundary \mathcal{B}_A . This reconstruction can be viewed as an image of the unknown conductivity σ , as we show below with numerical simulations. Moreover, as explained in section 2.4, the reconstruction mapping $\mathcal{Q}_n : \mathcal{D}_n \rightarrow \mathcal{S}$, from the set \mathcal{D}_n of discrete DtN maps to the set \mathcal{S} of positive and bounded conductivities, can be used as a preconditioner of the forward map

$$\mathcal{F}_n : \mathcal{S} \rightarrow \mathcal{D}_n, \quad \mathcal{F}_n(\sigma) = \mathcal{M}_n(\Lambda_\sigma), \quad (4.1)$$

in a Newton type iteration that solves the nonlinear minimization problem

$$\min_{\tilde{\sigma} \in \mathcal{S}} \|\mathcal{Q}_n \circ \mathcal{F}_n(\tilde{\sigma}) - \mathcal{Q}_n[\mathcal{M}_n(\Lambda_\sigma)]\|. \quad (4.2)$$

This iteration is studied in detail in [11, 49], and we do not repeat here.

The algorithm that computes the reconstruction \mathcal{Q}_n consists of the following steps:

Step 1. Compute the discrete DtN maps $\Lambda_\gamma = \mathcal{M}_n(\Lambda_\sigma)$ and $\Lambda_{\gamma^{(1)}} = \mathcal{M}_n(\Lambda_1)$ using the measurement operator \mathcal{M}_n defined in section 2.3. This implies choosing the odd number n of boundary measurements and the distribution of measurement points $e^{i\tau_k} \in \mathcal{B}_A$, for $k = 1, \dots, n$.

Step 2. Solve the discrete EIT problem for the circular resistor network with discrete DtN map Λ_γ computed at step 1. This gives the conductances $\gamma_{j,k}$ and $\hat{\gamma}_{j,k}$ of the resistors.

Step 3. Solve the discrete EIT problem for the circular resistor network with DtN map $\Lambda_{\gamma^{(1)}}$ computed at step 1, for the uniform conductivity $\sigma^{(1)} \equiv 1$. This gives the conductances $\gamma_{j,k}^{(1)}$ and $\hat{\gamma}_{j,k}^{(1)}$.

Step 4. Compute the extremal quasiconformal mapping T that takes the uniformly distributed points $e^{i\theta_k} \in \mathcal{B}$ to the measurement points $e^{i\tau_k} \in \mathcal{B}_A$,

$$e^{i\tau_k} = T(e^{i\theta_k}), \quad k = 1, \dots, n. \quad (4.3)$$

Use this mapping to compute the grid nodes $T(\widehat{r}_j e^{i\theta_k})$ and $T(r_j e^{i\widehat{\theta}_k})$, where r_j , \widehat{r}_j are the radii of the rotationally symmetric optimal grid, and $\theta_k = 2\pi(k-1)/n$, $\widehat{\theta}_k = 2\pi(k-1/2)/n$ are the equidistant angular grid nodes. In the particular case of τ_k distributed as in section 3.1, the mapping T is a conformal one.

Step 5. The reconstruction

$$\sigma^* = \mathcal{Q}_n[\mathcal{M}_n(\Lambda_\sigma)] \in \mathcal{S} \quad (4.4)$$

is given by the piecewise linear interpolation of the following values at the transformed grid nodes

$$\sigma^*(T(\widehat{r}_{j+m_{1/2}} e^{i\theta_k})) = \gamma_{j,k}/\gamma_{j,k}^{(1)}, \quad j = 1, \dots, m+1, \quad k = 1, \dots, n, \quad (4.5)$$

$$\sigma^*(T(r_j e^{i\widehat{\theta}_k})) = \widehat{\gamma}_{j,k}/\widehat{\gamma}_{j,k}^{(1)}, \quad j = 2 - m_{1/2}, \dots, m+1, \quad k = 1, \dots, n. \quad (4.6)$$

4.2. Numerical implementation

In step 1 of the inversion algorithm we choose the number n of boundary nodes. The choice of n is studied in [11, 49], and it is related to the amount of noise present in the measured data. Recall that the theory of discrete inverse problems for networks with circular planar graphs described in section 2.2 provides an exact relation between the number of boundary nodes and the number of layers of a uniquely recoverable network. The discrete EIT problem is exponentially ill-conditioned, losing roughly one digit of accuracy for each layer recovered. Hence the number of layers that can be stably recovered is limited by the noise level in the data, thus limiting n . A simple heuristic was proposed in [11, 49] to determine n by solving a sequence of discrete inverse problems for increasing n , until the layer peeling method [14] fails to produce positive conductances. In the numerical examples $n = 21$ ($m = 4$, $m_{1/2} = 1$), and it is well below the heuristic limit, which guarantees a stable solution of the discrete inverse problem.

We use measurement functions χ_k with small supports, so the size of the inaccessible boundary is slightly smaller than the image of the primary grid cell $(\theta_{(n+1)/2}, \theta_{(n+3)/2})$ that is mapped to \mathcal{B}_I according to (3.8). We take $\chi_k(\theta)$ as the indicator functions of intervals centered around the primary boundary grid nodes $e^{i\theta_k}$ and occupying 10% of the corresponding dual boundary grid interval. They are transformed to $\widetilde{\chi}_k(\tau) = \chi_k(g(\tau))$ by the boundary restriction g of the inverse of T . We indicate with small red squares the end points of the supports of $\widetilde{\chi}_k(\tau)$ in figures 9–13. Note that the measurements $\mathcal{M}_n(\Lambda_1)$ and $\mathcal{M}_n(\Lambda_\sigma)$ in steps 2 and 3 of the algorithm are computed using transformed functions $\widetilde{\chi}_k(\tau)$. The continuum DtN maps Λ_1 and Λ_σ are approximated with a finite difference scheme on a fine tensor product grid with 300 uniformly spaced nodes in angle and 100 uniformly spaced nodes in radius.

We solve the discrete inverse problems in steps 2 and 3 of the algorithm using the layer peeling method introduced in [14]. Being a direct method, the layer peeling is extremely fast, which makes our inversion algorithm computationally inexpensive. In fact, recovering all conductances in a network with layer peeling is faster than computing the Jacobian of the discrete DtN map with respect to the conductances. Thus, the layer peeling recovers the whole network faster than one iteration of

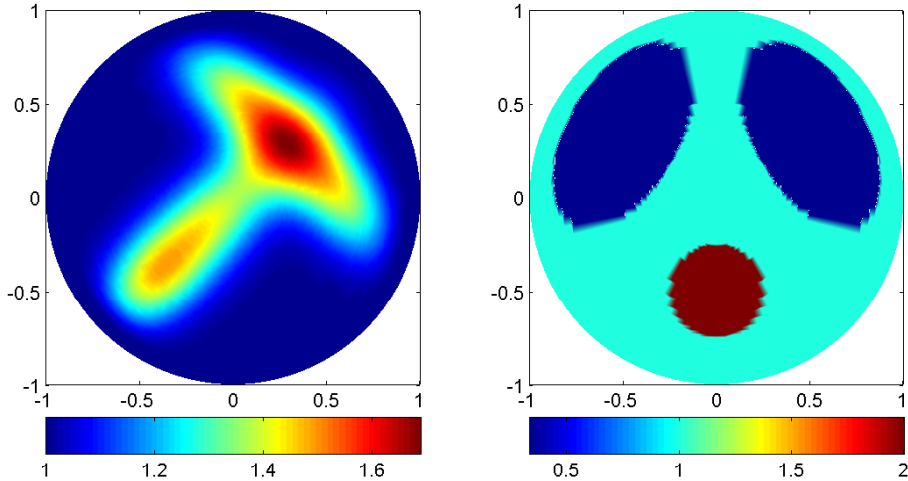


Figure 8. The conductivities used in the numerical experiments. Left: smooth conductivity $sigX$; right: piecewise constant chest phantom $phantom1$.

any gradient-based optimization method, which may take hundreds of iterations to converge considering the ill-conditioning of the problem.

Note that since the transformed measurement functions $\tilde{\chi}_k(\tau)$ are not rotationally symmetric in the sense of (2.15), the conductances $\gamma_{j,k}^{(1)}$ and $\hat{\gamma}_{j,k}^{(1)}$ obtained in step 3 depend on the angular index k , even though the conductivity $\sigma^{(1)} \equiv 1$ is rotationally invariant.

The Teichmüller mapping T in step 4 is computed using the decomposition (3.19) for a fixed value of the affine stretching constant K . Choosing K is a tradeoff between the resolution and the distortion of the reconstruction, as shown in the numerical examples below. The conformal mappings Φ and Ψ in decomposition (3.19) are computed numerically using the Schwartz-Christoffel toolbox [19]. In case $K = 0$ the mapping T is conformal, so we can use (3.5), with the parameters given by (3.9) to obtain $T = F$.

Recall from the numerical results in section 2.5 that the optimal grid depends weakly on the choice of averaging formulas and of the measurement operator. In all the numerical results presented below, we use the radii r_j, \hat{r}_j that correspond to log-averaging formulas and the measurement operator \mathcal{M}_n^* , for which these radii can be computed exactly (see Appendix A).

To compare the reconstructions for partial measurements with those for full boundary measurements, we present numerical results for the same conductivity functions considered in [11, 49]. They are shown in figure 8. The first one is a smooth conductivity ($sigX$), given by the superposition of two Gaussians. The second one is piecewise constant ($phantom1$), and it models a chest phantom [41].

It appears from the examples of optimal grids in figures 4 and 7, that the reconstructions will have better resolution near the accessible boundary. To explore this phenomenon, we rotate the accessible boundary (and therefore the grid) by ω_0

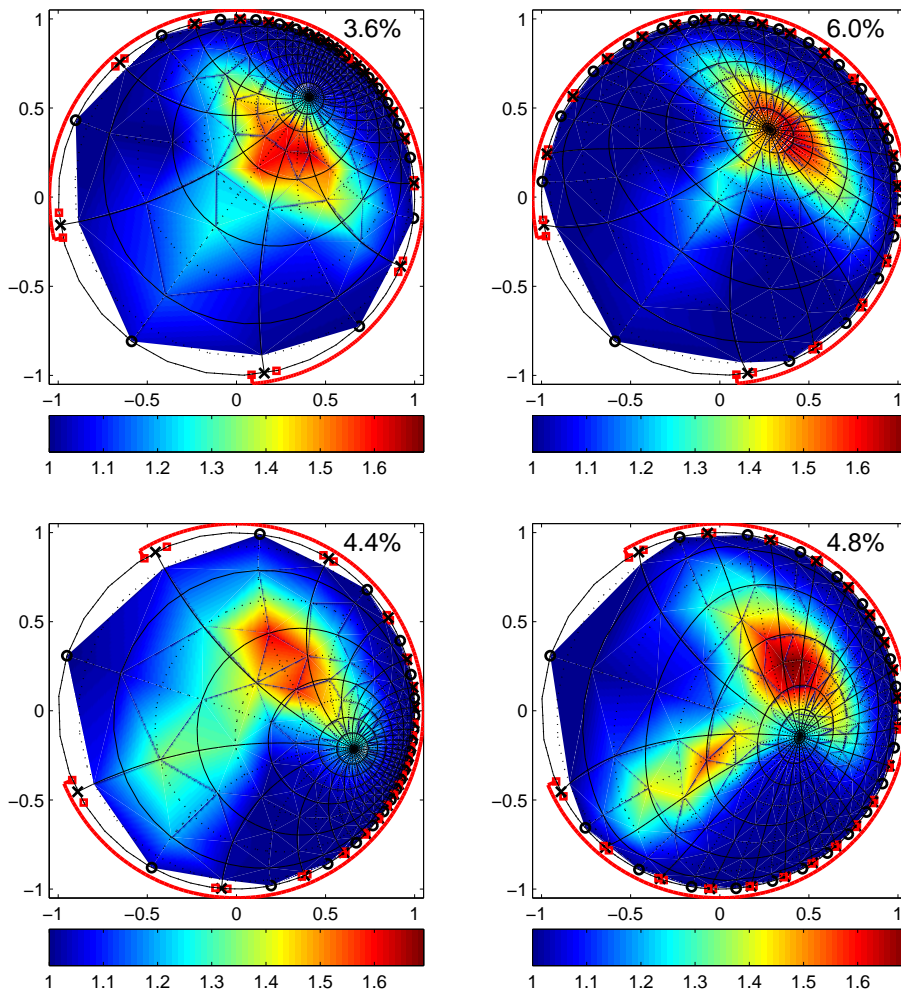


Figure 9. Reconstructions of the smooth conductivity $\text{sig}X$, $\beta = 3\pi/4$, $n = 21$. Top row: $\omega_0 = 3\pi/10$; bottom row: $\omega_0 = -\pi/10$. Left column: conformal mapping; right column: quasiconformal mapping, $K = 0.7$. \mathcal{B}_A is solid red. Percentages: mean relative errors $[E]$.

to move the high resolution region around the domain. Note that both $\text{sig}X$ and phantom1 have axes of symmetry. We specifically choose ω_0 so that the axis of symmetry of the grid $z = te^{i\omega_0}$, $t \in \mathbb{R}$, is neither collinear with nor orthogonal to the axis of symmetry of σ .

For each reconstruction we compute the pointwise relative error for every $z \in \mathbb{D}$ using the formula

$$E(z) = \left| \frac{\sigma^*(z)}{\sigma(z)} - 1 \right|. \quad (4.7)$$

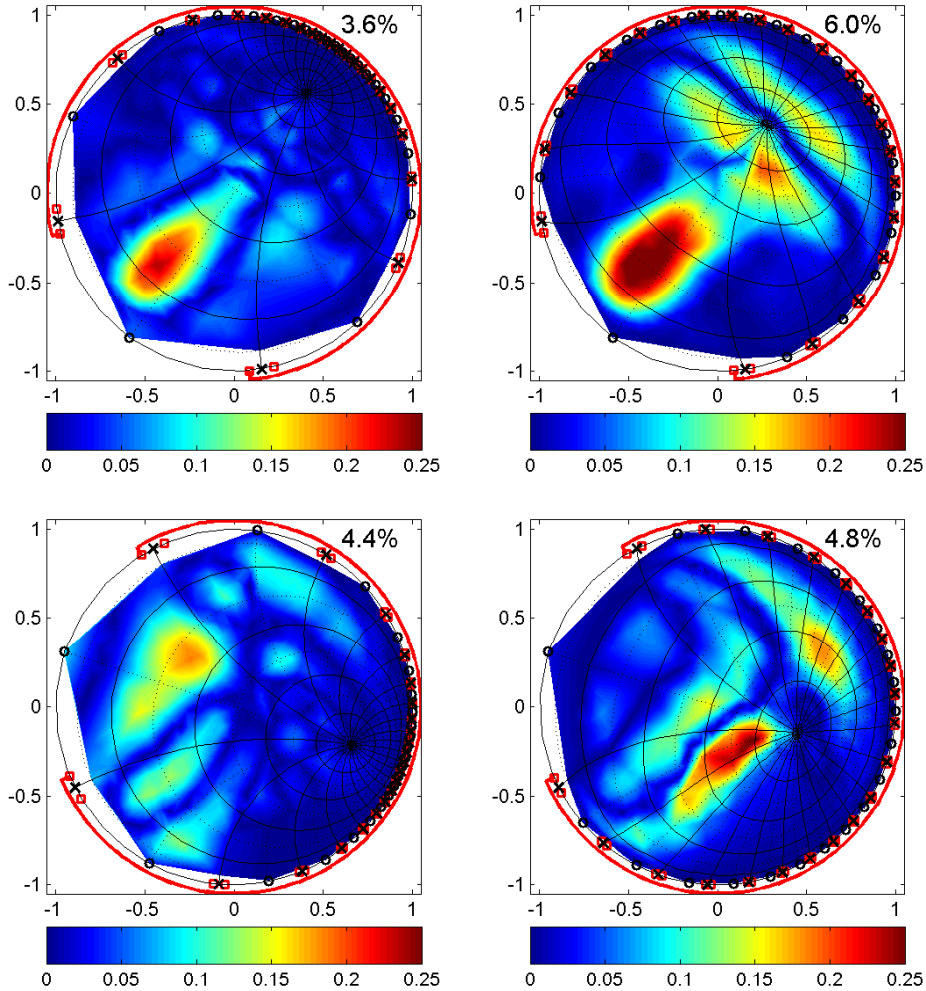


Figure 10. Pointwise relative error $E(z)$ for the reconstructions of the smooth conductivity $sigX$ given in figure 9. Percentages: mean relative errors $[E]$.

The mean relative error is

$$[E] = \frac{\int_H E(z) dz}{\int_H dz} \cdot 100\%, \quad (4.8)$$

where H is the convex hull of the optimal grid nodes, where the reconstruction $\sigma^*(z)$ is defined. We give $[E]$ in the top right corner of every reconstruction plot.

4.3. Reconstructions of smooth conductivity

We begin with reconstructions of the smooth conductivity $sigX$. In figure 9 we show reconstructions for two different values of ω_0 , which demonstrate how the resolution

of our method depends on the relative position of the accessible boundary and the features of the conductivity. We refer to the two distinct features of the hammer-like conductivity $\text{sig}X$ as the “head” and the “handle”.

For $\omega_0 = 3\pi/10$ the region of high resolution is close to the head feature for both the conformal and quasiconformal mapping reconstructions. As expected, the conformal mapping reconstruction loses quickly resolution away from the middle of the accessible boundary. The quasiconformal reconstruction has a more uniform resolution throughout the domain. However, we observe that the quasiconformal reconstruction is somewhat distorted compared to the true conductivity, which is the reason why it has a slightly larger mean relative error. We believe that this is a manifestation of the artificial anisotropy that is implicitly introduced by the quasiconformal mapping. Such distortions are observed for all reconstructions that we consider, both for the smooth and piecewise constant conductivities.

In the case $\omega_0 = -\pi/10$ the difference between the conformal and the quasiconformal reconstructions becomes more pronounced. The middle of the accessible boundary is away from both features of the conductivity, so the conformal mapping reconstruction is very coarse. The quasiconformal mapping reconstruction captures both features much better. However, similar to the case $\omega_0 = 3\pi/10$, we observe some distortion in the reconstruction, especially where the handle is connected to the head, which leads to a larger relative error compared to the conformal case.

The distribution of the relative error throughout \mathbb{D} for all four reconstructions of the smooth conductivity $\text{sig}X$ is given in figure 10. As expected, in the conformal case the error is small close to the middle of \mathcal{B}_A . The error in the quasiconformal case is concentrated around the features of the conductivity, which shows that the main source of error is the distortion.

4.4. Reconstructions of piecewise constant conductivity

Let us now consider the reconstructions of the piecewise constant chest phantom. Unlike in the smooth conductivity case, we study the behavior of the reconstructions not only for different values of ω_0 , but also for different choices of β . We refer to the low and high conductivity features of the phantom as the “lungs” and the “heart” respectively.

We show in figure 11 the reconstructions for $\omega_0 = -\pi/10$, and two sizes of the accessible boundary corresponding to $\beta = 4\pi/3$ and $\beta = 2\pi/3$, respectively. The middle of the accessible boundary is located close to the bottom of the right lung, and so the conformal mapping reconstruction captures the right lung quite well. However, the left lung is basically indistinguishable, and both the position and the conductivity value of the heart are captured poorly. The quasiconformal mapping reconstruction does a better job of imaging both the right lung and the heart, and even the left lung can be distinguished as a separate feature. This behavior becomes more pronounced as the accessible boundary is shrunk further.

The choice of ω_0 in figures 12 and 13 allows us to focus the reconstruction on the lungs and the heart respectively. We notice again that the conformal mapping reconstruction captures the geometry and the magnitude of the conductivity features in its high resolution region very well. None of the two approaches has a clear advantage over the other in terms of the relative error. Overall, the relative errors are higher for the reconstructions of the piecewise constant chest phantom than those for the smooth conductivity reconstruction. This is in part due to a behavior

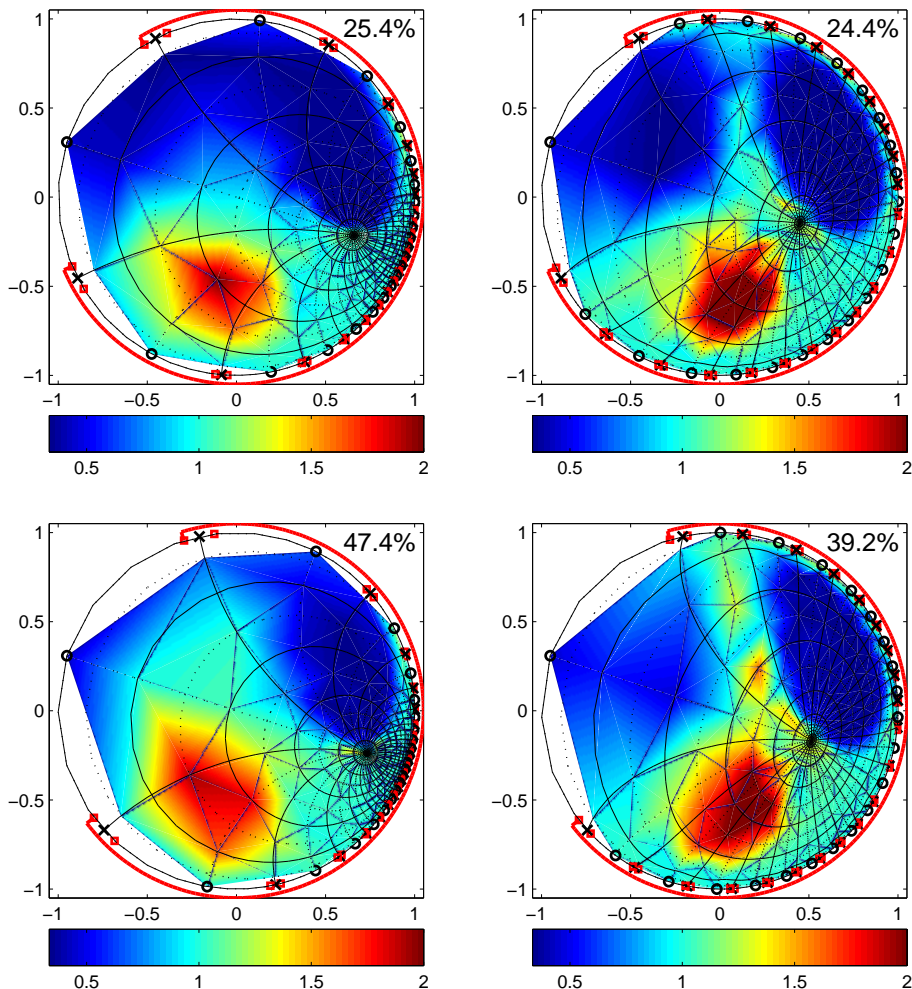


Figure 11. Reconstructions of piecewise constant conductivity *phantom1*, $\omega_0 = -\pi/10$, $n = 21$. Top row: $\beta = 3\pi/4$, $K = 0.7$; bottom row: $\beta = 2\pi/3$, $K = 0.63$. Left column: conformal mapping; right column: quasiconformal mapping. \mathcal{B}_A is solid red. Percentages: mean relative errors $[E]$.

similar to Gibbs phenomenon, which can be clearly observed in the quasiconformal reconstruction with $\beta = 2\pi/3$, $K = 0.63$ in figure 11. It manifests itself as a couple of spurious oscillations to the left from the right lung.

We can now conclude that both the conformal and quasiconformal approaches can be useful in different situations. If we have some a priori information on where the features of interest of the conductivity may be located, and if we have enough control over where the DtN map is measured, we can lump the measurements at the points prescribed by a conformal mapping, choosing the middle of the accessible boundary

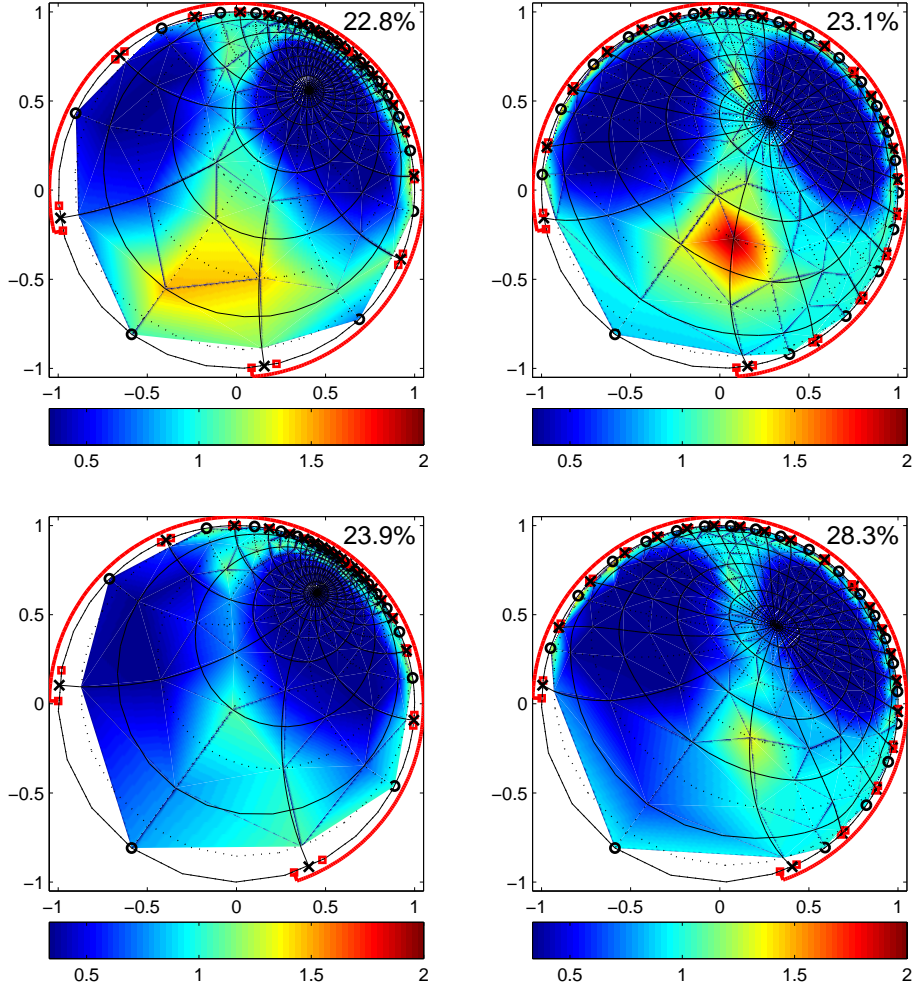


Figure 12. Reconstructions of piecewise constant conductivity *phantom1*, $\omega_0 = 3\pi/10$, $n = 21$. Top row: $\beta = 3\pi/4$, $K = 0.7$; bottom row: $\beta = 2\pi/3$, $K = 0.63$. Left column: conformal mapping; right column: quasiconformal mapping. \mathcal{B}_A is solid red. Percentages: mean relative errors $[E]$.

close to the suspected location of the features of interest. When no a priori information is available, or the accessible boundary is small, the quasiconformal approach is superior to the conformal one, because it has a better resolution throughout the domain.

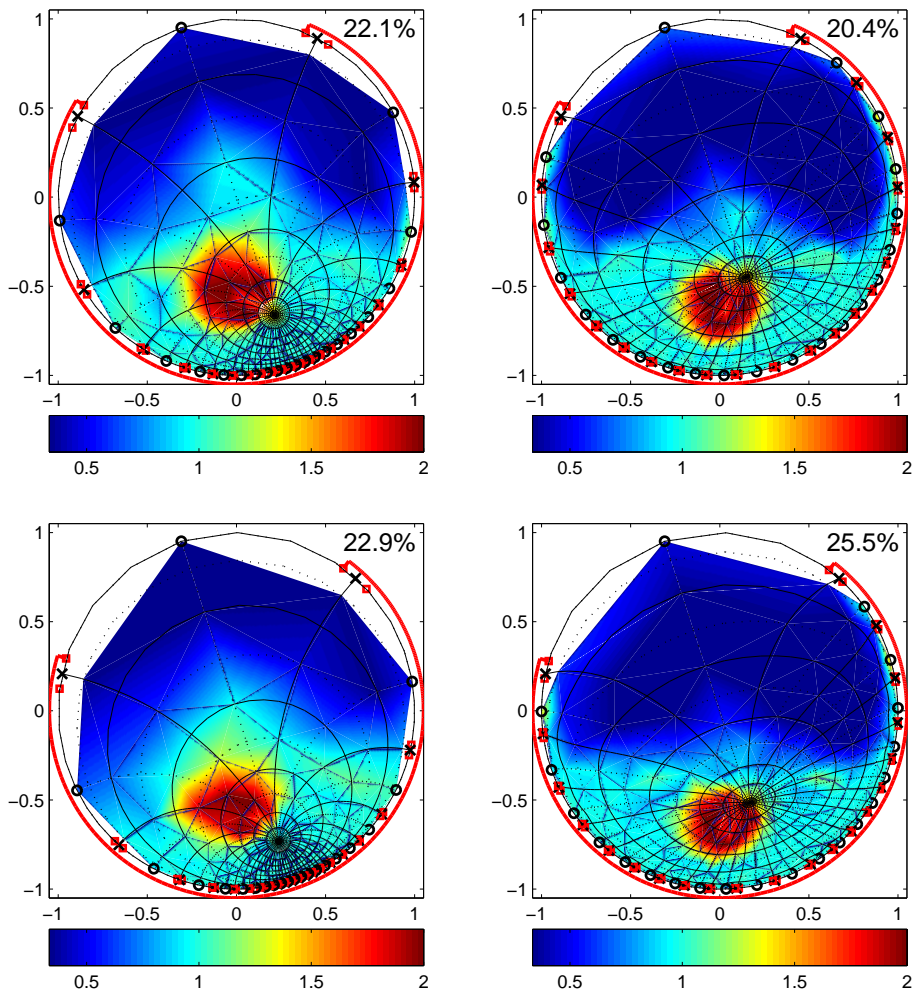


Figure 13. Reconstructions of piecewise constant conductivity *phantom1*, $\omega_0 = -2\pi/5$, $n = 21$. Top row: $\beta = 3\pi/4$, $K = 0.7$; bottom row: $\beta = 2\pi/3$, $K = 0.63$. Left column: conformal mapping; right column: quasiconformal mapping. \mathcal{B}_A is solid red. Percentages: mean relative errors $[E]$.

5. Summary

This paper is concerned with the extension of the two dimensional EIT inversion algorithm introduced in [11, 49] to the case of partial boundary measurements. The algorithm uses a model reduction approach that encodes the information about the unknown conductivity function σ in a few parameters. The reduced models are well connected, critical resistor networks that are consistent with discrete measurements of the Dirichlet-to-Neumann (DtN) map at n boundary points, and are uniquely

determined by them. The resistor networks arise in finite volume discretizations of the partial differential equation for the potential on staggered, so-called optimal grids that are computed as part of the inversion. The grids are called optimal because they give spectral accuracy of finite volume approximations of the DtN map on sparse grids (with few grid points). In particular, we compute them so that they compute exactly the action of specific measurement operators on the DtN map Λ_1 , for constant conductivity $\sigma \equiv 1$.

The optimal grids are the key to the connection between the continuum EIT problem and the discrete reduced models, the resistor networks. It is shown in [11, 49] that they have nice extrapolation properties for a class of conductivity functions that contains $\sigma \equiv 1$. That is, when we compute the grids to reproduce exactly the measurements of Λ_1 , they also approximate very well the measurements of Λ_σ , for $\sigma \neq 1$. This is why we can use them to define a reconstruction mapping \mathcal{Q}_n that takes the measurements and returns an approximation of the conductivity.

The optimal grids for EIT with full boundary measurements are constructed in [11, 49] based on the rotational symmetry of the problem in the disk \mathbb{D} , and for $\sigma \equiv 1$. They are tensor product grids with uniform angular discretization and optimally determined radial layers. The grids are staggered and refined near the boundary, where we make the measurements and we expect the best resolution of the reconstructions. These were observations of numerical results in [11, 49], but we prove them here.

The EIT problem with partial boundary measurements is not rotationally symmetric, so it is not immediately clear how to define the optimal grids from the construction in [11, 49]. The main result of this paper is the construction of the optimal grids and of the mapping \mathcal{Q}_n for EIT with partial boundary measurements, using extremal quasiconformal (Teichmüller) mappings. The idea is to map the problem with n partial measurements on the accessible part \mathcal{B}_A of the boundary \mathcal{B} , to the problem with n equidistantly distributed measurements on the entire \mathcal{B} . The latter is the problem with full boundary measurements, which can be solved as in [11, 49], using the transformed measurements.

There are many diffeomorphisms of the disk \mathbb{D} to itself, but in general they transform the unknown conductivity σ to an anisotropic, matrix valued $\tilde{\sigma}$. Matrix valued conductivities are not uniquely determined by the transformed (push forward) DtN map, so it seems that we should restrict the mappings to conformal ones, which preserve the isotropy of σ under the transformation. We show however that such mappings may not be the best choice, because they correspond to very special distributions of the measurement points, which are clustered in the center of the accessible region. Therefore, the conformal grids are refined near the center of \mathcal{B}_A and the reconstructions have poor resolution in the remainder of the domain. In order to get better resolution in a larger part of the domain, and to measure at more general distributions of n points in \mathcal{B}_A , we must introduce some anisotropy in the problem. This is why we use extremal quasiconformal (Teichmüller) mappings, which transform the EIT problem with partial measurements for the unknown σ to an EIT problem with full boundary measurements for a transformed $\tilde{\sigma}$ that is anisotropic, but has minimum and uniform anisotropy.

An interesting conclusion of our study is that the distribution of boundary points in \mathcal{B}_A has a strong effect on the reconstructions. There is a trade-off between achieving very good reconstructions in a small region near the middle of \mathcal{B}_A and having resolution spread out more uniformly in \mathbb{D} . The former is best achieved by grids obtained with

conformal mappings or at least by Teichmüller mappings with almost zero dilatation parameter. They require an accumulation of the measurement points in the center of \mathcal{B}_A . When the measurement points are spread out throughout \mathcal{B}_A , the quasiconformal grids give better resolution throughout \mathbb{D} , but they produce a reconstruction mapping \mathcal{Q}_n with some distortion, due to the artificial anisotropy. This is in fact a consequence of the topology of the grids and resistor networks, and it may be circumvented by considering different topologies, as shown in [39] and in a forthcoming article [10].

We end with the observation that since we proved that the optimal grids for the EIT problem with full boundary measurements are refined near the boundary and staggered, we can conclude the same about the grids for partial measurements. This is because the grids are transformations of each other via diffeomorphisms. This fact is also illustrated in the numerical results.

Acknowledgements

The work of L. Borcea was partially supported by the National Science Foundation, grants DMS-0604008, DMS-0934594, DMS-0907746 and by the Office of Naval Research grant N000140910290. The work of A. Mamonov was partially supported by the National Science Foundation, grants DMS-0604008, DMS-0934594 and by Schlumberger Technology Corporation under the research agreement R62860.

Appendix A. Alternative measurement and averaging formulas

Recall from section 2.4 that the case of layered conductivity $\sigma(r, \theta) = \sigma(r)$ has a particular importance for the construction of the optimal radial grids for the uniform discretization in angle. From the rotational symmetry of the layered problem it follows that $e^{ik\theta}$ are the eigenfunctions of the DtN map

$$\Lambda_\sigma e^{ik\theta} = R_\sigma(k) e^{ik\theta}, \quad k \in \mathbb{Z}, \quad (\text{A.1})$$

where the eigenvalues $R_\sigma(k) = R_\sigma(-k) > 0$ are given in terms of the *admittance* function R_σ , which can be extended to the whole complex plane in terms of the spectral measure of the differential operator (1.1). A trivial calculation in the case $\sigma \equiv 1$ shows that

$$R_1(\lambda) = |\lambda|. \quad (\text{A.2})$$

Thus, we can formally write

$$\Lambda_1 = \sqrt{-\frac{\partial^2}{\partial \theta^2}}. \quad (\text{A.3})$$

In what follows it is convenient to define $\beta_\sigma(\lambda) = R_\sigma(\lambda)/|\lambda|$.

Our goal is to derive a discrete analogue of (A.3), which is possible if we introduce a measurement operator \mathcal{M}_n^* defined below. Instead of using a single set of measurement functions χ_k , we consider two families ζ_k and η_j , where ζ_k are the eigenfunctions of Λ_σ , and η_j are the indicator functions of intervals $(\hat{\theta}_j, \hat{\theta}_{j+1})$. Then the vector of measured currents $J^{(k)}$ is given by

$$J_j^{(k)} = \int_0^{2\pi} \eta_j(\theta) (\Lambda_\sigma \zeta_k)(\theta) d\theta = \beta_\sigma(k) \int_{\frac{2\pi}{n}(j-1/2)}^{\frac{2\pi}{n}(j+1/2)} |k| e^{ik\theta} d\theta, \quad (\text{A.4})$$

where $j = 1, \dots, n$ and $k = -(n-1)/2, \dots, (n-1)/2$.

Let $\zeta_j^{(k)} = \zeta_k(\theta_j) = e^{i\frac{2\pi kj}{n}}$ be the components of the vector of boundary potential at the primary grid nodes. The action of the measurement operator $\mathcal{M}_n^*(\Lambda_\sigma)$ on vectors $\zeta^{(k)}$ is

$$\mathcal{M}_n^*(\Lambda_\sigma)\zeta^{(k)} = J^{(k)}. \quad (\text{A.5})$$

Rewriting (A.4) we observe that

$$J_j^{(k)} = 2\beta_\sigma(k) \left| \sin\left(\frac{\pi k}{n}\right) \right| e^{i\frac{2\pi kj}{n}}. \quad (\text{A.6})$$

Using notation $\omega_k^{(n)} = 2|\sin(\pi k/n)|$ we finally arrive at

$$\mathcal{M}_n^*(\Lambda_\sigma)\zeta^{(k)} = \beta_\sigma(k)\omega_k^{(n)}\zeta^{(k)}, \quad k = -\frac{n-1}{2}, \dots, \frac{n-1}{2}. \quad (\text{A.7})$$

Let us define a symmetric circulant matrix $\Delta^{(n)} \in \mathbb{R}^{n \times n}$ with the entries

$$\Delta_{i,j}^{(n)} = -2\delta_{i,j} + \delta_{i+1,j} + \delta_{i,j+1} + \delta_{i,1}\delta_{j,n} + \delta_{i,n}\delta_{j,1}. \quad (\text{A.8})$$

Up to a scaling factor $1/h_\theta^2$ (A.8) is a finite difference discretization of the second derivative on a three point stencil at equidistant nodes θ_j . Since $\Delta^{(n)}$ is circulant, its eigenvectors are $\zeta^{(k)}$ and its eigenvalues λ_k are the discrete Fourier transform of its first column

$$\lambda_k = -2 + e^{i\frac{2\pi k}{n}} + e^{-i\frac{2\pi k}{n}} = -(\omega_k^{(n)})^2. \quad (\text{A.9})$$

Combining (A.7) with (A.9) it is easy to observe that (A.7) for $\sigma \equiv 1$ ($\beta_1 \equiv 1$) is a discrete analogue of (A.3)

$$\mathcal{M}_n^*(\Lambda_1) = \sqrt{-\Delta^{(n)}}. \quad (\text{A.10})$$

It follows from the results of [28] that $\mathcal{M}_n^*(\Lambda_\sigma)$ is a DtN map of a resistor network, and in the case $\sigma \equiv 1$ the conductances admit an analytic expression

$$\gamma_j^{(1)} = \tan\left(\frac{\pi(2m+3-2j)}{n}\right), \quad j = 1, \dots, m+1, \quad (\text{A.11})$$

$$\widehat{\gamma}_j^{(1)} = \cot\left(\frac{\pi(2m+4-2j)}{n}\right), \quad j = 2 - m_{1/2}, \dots, m+1, \quad (\text{A.12})$$

as shown in [5].

Expressions (A.11)–(A.12) allow us to establish the interlacing and refinement properties of the optimal grids. It is easier to do so for the log-averaging formulas used in [11, 49] instead of the averaging formulas (2.18)–(2.19). The log-averaging formulas are

$$\gamma_{j,k} = \sigma(\widehat{r}_{j+m_{1/2}}, \theta_k) \frac{h_\theta}{\log\left(\frac{r_j}{r_{j+1}}\right)}, \quad j = 1, \dots, m+1, \quad k = 1, \dots, n, \quad (\text{A.13})$$

$$\widehat{\gamma}_{j,k} = \sigma(r_j, \widehat{\theta}_k) \frac{\log\left(\frac{\widehat{r}_{j+m_{1/2}-1}}{\widehat{r}_{j+m_{1/2}}}\right)}{h_\theta}, \quad j = 2 - m_{1/2}, \dots, m+1, \quad k = 1, \dots, n. \quad (\text{A.14})$$

The radii of the optimal grid take the form

$$r_{j+1} = \exp\left(-h_\theta \sum_{s=1}^j \frac{1}{\gamma_s^{(1)}}\right), \quad j = 1, \dots, m+1 \quad (\text{A.15})$$

$$\widehat{r}_{j+m_{1/2}} = \exp\left(-h_\theta \sum_{s=2-m_{1/2}}^j \widehat{\gamma}_s^{(1)}\right), \quad j = 2 - m_{1/2}, \dots, m+1. \quad (\text{A.16})$$

Note, that according to (A.11)–(A.12) the conductances form a monotone interlacing sequence in the sense of

$$(\widehat{\gamma}_1^{(1)}) < \frac{1}{\gamma_1^{(1)}} < \widehat{\gamma}_2^{(1)} < \frac{1}{\gamma_2^{(1)}} < \dots < \widehat{\gamma}_{m+1}^{(1)} < \frac{1}{\gamma_{m+1}^{(1)}}. \quad (\text{A.17})$$

Summing (A.17) we can perform transformations

$$-h_\theta \sum_{s=1}^j \frac{1}{\gamma_s^{(1)}} > -h_\theta \sum_{s=1}^j \widehat{\gamma}_{s+1}^{(1)} > -h_\theta \sum_{s=1}^j \frac{1}{\gamma_{s+1}^{(1)}}, \quad (\text{A.18})$$

$$-h_\theta \sum_{s=1}^j \frac{1}{\gamma_s^{(1)}} > -h_\theta \sum_{s=2}^{j+1} \widehat{\gamma}_s^{(1)} - h_\theta m_{1/2} \widehat{\gamma}_1^{(1)} > -h_\theta \sum_{s=2}^{j+1} \frac{1}{\gamma_s^{(1)}} - h_\theta m_{1/2} \widehat{\gamma}_1^{(1)}, \quad (\text{A.19})$$

$$-h_\theta \sum_{s=1}^j \frac{1}{\gamma_s^{(1)}} > -h_\theta \sum_{s=2-m_{1/2}}^{j+1} \widehat{\gamma}_s^{(1)} > -h_\theta \sum_{s=2}^{j+1} \frac{1}{\gamma_s^{(1)}} - h_\theta \frac{1}{\gamma_1^{(1)}}, \quad (\text{A.20})$$

which become after the exponentiation the interlacing condition

$$r_{j+1} > \widehat{r}_{j+2} > r_{j+2}. \quad (\text{A.21})$$

A similar argument can be used to show grid refinement $\frac{r_j}{r_{j+1}} < \frac{r_{j+1}}{r_{j+2}}$.

References

- [1] G. Alessandrini. Stable determination of conductivity by boundary measurements. *Applicable Analysis*, 27(1):153–172, 1988.
- [2] K. Astala and L. Päivärinta. Calderón’s inverse conductivity problem in the plane. *Annals of Mathematics-Second Series*, 163(1):265–300, 2006.
- [3] S. Asvadurov, V. Druskin, and L. Knizhnerman. Application of the difference Gaussian rules to solution of hyperbolic problems. *Journal of Computational Physics*, 158(1):116–135, 2000.
- [4] J.A. Barcelo, T. Barcelo, and A. Ruiz. Stability of the inverse conductivity problem in the plane for less regular conductivities. *Journal of Differential Equations*, 173(2):231–270, 2001.
- [5] O.D. Biesel, D.V. Ingerman, J.A. Morrow, and W.T. Shore. Layered Networks, the Discrete Laplacian, and a Continued Fraction Identity. <http://www.math.washington.edu/~reu/papers/current/william/layered.pdf>.
- [6] L. Borcea. Electrical impedance tomography. *Inverse Problems*, 18(6):99–136, 2002.
- [7] L. Borcea and V. Druskin. Optimal finite difference grids for direct and inverse Sturm-Liouville problems. *Inverse Problems*, 18(4):979–1002, 2002.
- [8] L. Borcea, V. Druskin, and L. Knizhnerman. On the Continuum Limit of a Discrete Inverse Spectral Problem on Optimal Finite Difference Grids. *Communications on Pure and Applied Mathematics*, 58(9):1231, 2005.
- [9] L. Borcea, V. Druskin, and A. Mamonov. Solving the discrete EIT problem with optimization techniques, 2007. Schlumberger-Doll Report.
- [10] L. Borcea, V. Druskin, A.V. Mamonov, and F.G. Vasquez. Pyramidal resistor networks for electrical impedance tomography with partial boundary measurements. Preprint to be submitted to *Inverse Problems*, 2009.
- [11] L. Borcea, V. Druskin, and F.G. Vasquez. Electrical impedance tomography with resistor networks. *Inverse Problems*, 24(3):035013 (31pp), 2008.
- [12] A.L. Bukhgeim and G. Uhlmann. Recovering a potential from partial Cauchy data. *Communications in Partial Differential Equations*, 27(3):653–668, 2002.
- [13] A.P. Calderón. On an inverse boundary value problem, Seminar on Numerical Analysis and its Applications to Continuum Physics, Soc. *Brasileira de Matematica, Rio de Janeiro*, pages 65–73, 1980.
- [14] E. Curtis, E. Mooers, and J.A. Morrow. Finding the conductors in circular networks from boundary measurements. *RAIRO - Mathematical Modelling and Numerical Analysis*, 28:781–814, 1994.
- [15] E.B. Curtis, D. Ingerman, and J.A. Morrow. Circular planar graphs and resistor networks. *Linear Algebra and its Applications*, 23:115–150, 1998.

- [16] I. Daubechies, M. Defrise, and C. De Mol. An iterative thresholding algorithm for linear inverse problems with a sparsity constraint. *Communications on Pure and Applied Mathematics*, 57:1413–57, 2004.
- [17] Y.C. de Verdière. Réseaux électriques planaires I. *Commentarii Mathematici Helvetici*, 69(1):351–374, 1994.
- [18] Y.C. de Verdière, I. Gitler, and D. Vertigan. Réseaux électriques planaires II. *Commentarii Mathematici Helvetici*, 71(1):144–167, 1996.
- [19] T.A. Driscoll. Schwarz-Christoffel Toolbox Users Guide: Version 2.3, 2002. Department of Mathematical Sciences, University of Delaware, Newark, DE.
- [20] T.A. Driscoll and L.N. Trefethen. *Schwarz-Christoffel Mapping*. Cambridge University Press, 2002.
- [21] V. Druskin. The unique solution of the inverse problem of electrical surveying and electrical well-logging for piecewise-continuous conductivity. *Izv. Earth Physics*, 18:51–3, 1982.
- [22] V. Druskin. On uniqueness of the determination of the three-dimensional underground structures from surface measurements with variously positioned steady-state or monochromatic field sources. *Sov. Phys.–Solid Earth*, 21:210–4, 1985.
- [23] V. Druskin and L. Knizhnerman. Gaussian spectral rules for second order finite-difference schemes. *Numerical Algorithms*, 25(1):139–159, 2000.
- [24] V. Druskin and L. Knizhnerman. Gaussian spectral rules for the three-point second differences: I. A two-point positive definite problem in a semi-infinite domain. *SIAM Journal on Numerical Analysis*, 37(2):403–422, 2000.
- [25] H.W. Engl, M. Hanke, and A. Neubauer. *Regularization of inverse problems*. Kluwer Academic Pub, 1996.
- [26] H. Heck and J. Wang. Stability estimates for the inverse boundary value problem by partial Cauchy data. *Inverse Problems*, 22(5):1787, 2006.
- [27] O.Y. Imanuvilov, G. Uhlmann, and M. Yamamoto. Global uniqueness from partial Cauchy data in two dimensions. *Arxiv preprint arXiv:0810.2286*, 2008.
- [28] D. Ingerman. Discrete and continuous Dirichlet-to-Neumann maps in the layered case. *SIAM Journal on Mathematical Analysis*, 31:1214–1234, 2000.
- [29] D. Ingerman, V. Druskin, and L. Knizhnerman. Optimal finite difference grids and rational approximations of the square root I. Elliptic problems. *Communications on Pure and Applied Mathematics*, 53(8):1039–1066, 2000.
- [30] D. Ingerman and J. A. Morrow. On a characterization of the kernel of the Dirichlet-to-Neumann map for a planar region. *SIAM Journal on Applied Mathematics*, 29:106–115, 1998.
- [31] D. Isaacson. Distinguishability of conductivities by electric current computed tomography. *IEEE transactions on medical imaging*, 5(2):91–95, 1986.
- [32] K. Knudsen, M. Lassas, J. Mueller, and S. Siltanen. Regularized D-bar method for the inverse conductivity problem. *Inverse Problems and Imaging*, 3(4):599–624, 2009.
- [33] R. Kohn and M. Vogelius. Determining conductivity by boundary measurements. *Communications on Pure and Applied Mathematics*, 37:289–98, 1984.
- [34] R. Kohn and M. Vogelius. Determining conductivity by boundary measurements II. Interior results. *Communications on Pure and Applied Mathematics*, 38(5), 1985.
- [35] V. Kolehmainen, M. Lassas, and P. Ola. Inverse conductivity problem with an imperfectly known boundary. *Arxiv preprint math.AP/0408237*, 2004.
- [36] M.A. Lavrentiev and B.V. Shabat. *Methods of the complex variable function theory (in Russian)*. Nauka, Moscow, 1987.
- [37] H.R. MacMillan, T.A. Manteuffel, and S.F. McCormick. First-order system least squares and electrical impedance tomography: part II. To appear.
- [38] H.R. MacMillan, T.A. Manteuffel, and S.F. McCormick. First-order system least squares and electrical impedance tomography. *SIAM Journal on Numerical Analysis*, 42(2):461–483, 2004.
- [39] A.V. Mamonov. Resistor Network Approaches to the Numerical Solution of Electrical Impedance Tomography with Partial Boundary Measurements. Master’s thesis, Rice University, Houston, TX, USA, 2009.
- [40] N. Mandache. Exponential instability in an inverse problem for the Schrodinger equation. *Inverse Problems*, 17(5):1435–1444, 2001.
- [41] J.L. Mueller, S. Siltanen, and D. Isaacson. A direct reconstruction algorithm for electrical impedance tomography. *IEEE Trans. Med. Imaging*, 21(6):555–559, 2002.
- [42] A.I. Nachman. Global uniqueness for a two-dimensional inverse boundary value problem. *Annals of Mathematics*, pages 71–96, 1996.
- [43] E. Reich. Quasiconformal mappings of the disk with given boundary values. *Lecture Notes in*

- Mathematics*, 505:101–137, 1976.
- [44] E. Reich and K. Strebel. Extremal plane quasiconformal mappings with given boundary values. *American Mathematical Society*, 79(2), 1973.
 - [45] K. Strebel. On the existence of extremal Teichmüller mappings. *Journal d'Analyse Mathématique*, 30(1):464–480, 1976.
 - [46] K. Strebel. Extremal quasiconformal polygon mappings for arbitrary subdomains of compact Riemann surfaces. In *Annales Academiæ Scientiarum Fennicæ Mathematica*, volume 27, pages 237–248. Academia Scientiarum Fennica, 2002.
 - [47] J. Sylvester. An anisotropic inverse boundary value problem. *Communications on Pure and Applied Mathematics*, 43(2):201–232, 1990.
 - [48] J. Sylvester and G. Uhlmann. A global uniqueness theorem for an inverse boundary value problem. *Annals of Mathematics*, 125(1):153–169, 1987.
 - [49] F.G. Vasquez. *On the Parametrization of Ill-posed Inverse Problems Arising from Elliptic Partial Differential Equations*. PhD thesis, Rice University, Houston, TX, USA, 2006.